Structural and Thermal Diffusivity Analysis of an Organoferroelastic Crystal Showing Scissor-Like Two-Directional Deformation Induced by Uniaxial Compression

Subham Ranjan, Meguya Ryu, Ryota Morioka, Shuji Kamegaki, Soon Hock Ng, Daniel Smith, Jitraporn Vongsvivut, Mark J. Tobin, Saulius Juodkazis, Junko Morikawa,* and Satoshi Takamizawa*

Read Online

ACCESS | Metrics & More | Article Recommendations | SI Supporting Information

ABSTRACT: A two-directional ferroelastic deformation in organic crystals is unprecedented owing to its anisotropic crystal packing, in contrast to isotropic symmetrical packing in inorganic compounds and polymers. Thereby, finding and constructing multidirectional ferroelastic deformations in organic compounds is undoubtedly complex and at once calls for deep comprehension. Herein, we demonstrate the first example of a two-directional ferroelastic deformation with a unique scissor-like movement in single crystals of *trans*-3-hexenedioic acid by the application of uniaxial compression stress. A detailed structural investigation of the mechanical deformation at the macroscopic and microscopic levels by three distinct force measurement techniques (including shear and three-point bending test), single crystal X-ray diffraction techniques, and polarized synchrotron-FTIR microspectroscopy highlighted that mechanical twinning promoted the deformation. The presence of two crystallographically equivalent faces and the herringbone arrangement promoted the two-directional ferroelastic deformation. In addition, anisotropic heat transfer properties in the parent and the deformed domains were investigated by thermal diffusivity measurement on all three axes using microscale temperature-wave analysis (μ-TWA). A correlation between the anisotropic structural arrangement and the difference in thermal diffusivity and mechanical behavior in the two-directional organoferroelastic deformation could be established. The structural and molecular level information from this two-directional ferroelastic deformation would lead to a more profound understanding of the structure−property relationship in multidirectional deformation in organic crystals.
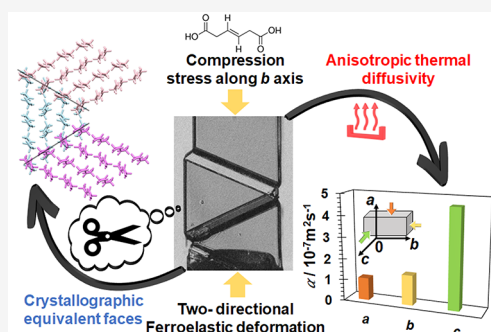
INTRODUCTION

Flexibility and shape change behavior of organic crystals induced by various external stimuli such as mechanical stress,[1,2] temperature,[3] or light[4] has received immense attention in the field of material science. The preconceived notion of such mechanical behaviors, which are typically limited to inorganic materials and polymers, is now shattered, and organic molecular crystals are considered an alternative structural material with the added benefits of low cost, easy processing, biocompatibility, and environmental friendliness.[5] Various mechanical deformations in organic crystals, such as elastic,[6−8] plastic,[9−12] superelastic,[13−16] ferroelastic,[17−20] shape memory effect,[21,22] and various others[23−27] have been explored. Among these deformations, ferroelasticity exhibits ferroic properties in response to mechanical stress, similar to ferroelectricity and ferromagnetism. A ferroelastic crystal is characterized by the presence of two or more stable orientational states/domains in the absence of mechanical stress.[28] The different orientational states can be reverted to one another by the application of mechanical stress, resulting in a reversible diffusionless phase transformation. So far, it has been observed that different domains in an organic ferroelastic crystal arise due to the development of spontaneous strain caused by twinning.[29,30] Mechanical twinning or twinning caused by shear stress is generated by the orientational change of the molecules, while maintaining single-molecule-to-single-molecule correspondence with the initial (mother) domain.[17,27,31,32] Thereby, the reversible diffusionless transformation of ferroelastic crystals differentiates it from irreversible plastic bending caused by dislocation, defects, or activation of multiple slip planes. This reversible trait of ferroelastic materials is exploited to develop switchable materials for energy conversion, memory storage, and mechanical switches.[5,33,34]

The evidence is increasing that ferroelastic materials are desirable candidates for switchable electronics, owing their mechanical and thermal properties to the phase-changing
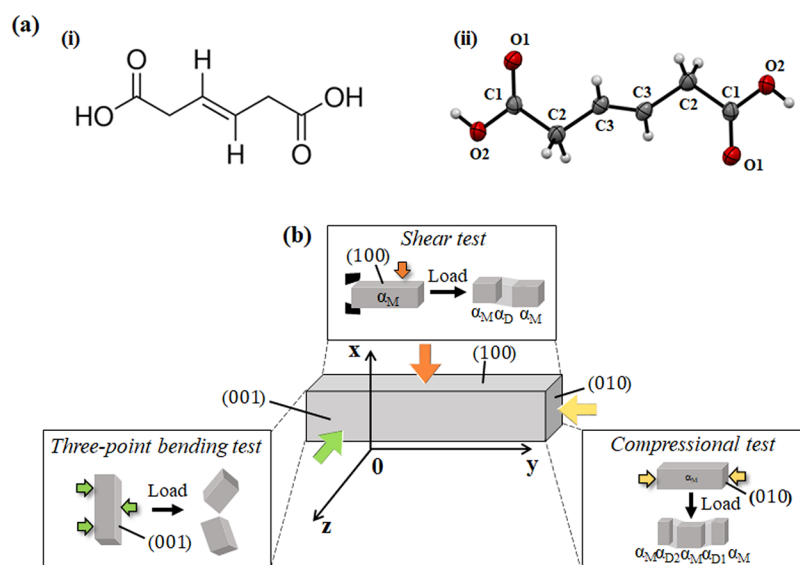
Figure 1. (a, i) Molecular structure of *trans*-3-hexanedioic acid and (ii) its ORTEP view in the crystal of **1**. (b) Schematic illustration of the crystal with its face indexes and the corresponding deformation test. The orange, yellow, and green denote the application of shear force, compressional force, and a three-point bending test, respectively.

behavior of ferroelastic materials under strain.[20,35,36] Understanding the structural aspect of organic crystals manifesting the mechanical deformation property is critical for progressing to the next step of the rational design of crystals with superior deformation behavior. However, ferroelasticity in organic crystals is limited to direction-dependent deformation, because of anisotropic interactions and low symmetry space groups. On the other hand, inorganic compounds and polymers with isotropic bonding interactions and symmetrical space groups exhibit direction-independent deformation behavior. The flexibility requirements of electronic/optoelectronic devices can be met by two-directional ferroelastic materials.[32] Thus, finding and studying the structure−property relationship in two-directional ferroelastic organic crystals are highly warranted. Only a handful of studies have been published on two-dimensional or multidirectional mechanical deformations of organic molecular crystals. Saha and Desiraju[26] described a strategy for designing two-dimensional (2D) elastic and plastic crystals by manipulating strong hydrogen bonds and weak halogen bonds in mutually orthogonal orientations. In line with this research, we discovered that the 2D side-to-end synthon generated by the halogen bond in one direction and the weak hydrogen bond at its perpendicular end aided the 2D ferroelastic deformation in our previous report of the two-dimensional ferroelastic crystal of 4-iodoaniline.[37] However, all of these studies describe shear force-induced deformation, which allows for the detection of just one directional deformation at a time. Ferroelastic deformation in organic molecular crystals caused by uniaxial compression has not yet been reported. Uniaxial compression tests would provide information about the plastic behavior of materials beyond their elastic limit, which is important for practical applications such as optoelectronics, mechanical/thermal switches, and energy storage devices.

On another note, ferroelastic materials are desirable candidates for switchable electronics and mechanical and thermal properties owing to the phase-changing behavior of ferroelastic materials under strain. Controlling thermal transport properties such as thermal diffusivity and thermal conductivity through the phase change in ferroelastic materials can deepen

the understanding of thermal management and helps in further design and development of such materials.[38,39] As a consequence, studying the anisotropic thermal transport properties and their relationship with crystal structural interactions in organic ferroelastic properties becomes of paramount importance.

On that account, we focused on finding two-directional ferroelasticity in organic crystals, studying their thermal transport properties, and understanding the underlying mechanism through crystallographic analysis. Herein, we report the first example of two-directional ferroelastic deformation under uniaxial compressive stress in the organic crystals of *trans*-3-hexanedioic acid (hereafter named as **1**). On application of uniaxial compressive stress, a unique two-directional ferroelastic deformation with a scissor-like movement was observed. The underlying mechanism of the two-directional deformation was elucidated by single crystal X-ray diffraction analysis. Further, the anisotropic thermal properties, i.e., thermal diffusivity values on the three-principal axes, were measured at a microscopic level by microscopic temperature wave analysis (μ-TWA). The relationship between mechanical and thermal properties was elucidated by crystal packing and energy framework analysis. Polarized synchrotron-FTIR microspectroscopy was applied to analyze the domain structure of this ferroelastic crystal.

■ RESULTS AND DISCUSSION

Preparation and Characterizations of Single Crystals. The slow evaporation process of *trans*-3-hexanedioic acid from its methanol solvent yielded block-shaped crystals of **1**, which were then used to examine the ferroelastic deformation behavior. The single crystal of **1** exhibited a melting endotherm at 198 °C in the differential scanning calorimetry (DSC) thermogram (Figure S1, Supporting Information (SI)). Negligible weight loss was observed prior to the melting point in its thermogravimetric profile, confirming the thermal stability at room temperature (RT). Thus, deformation tests and single-crystal X-ray diffraction data of the obtained crystal of **1** (Figure 1a) were collected at RT.
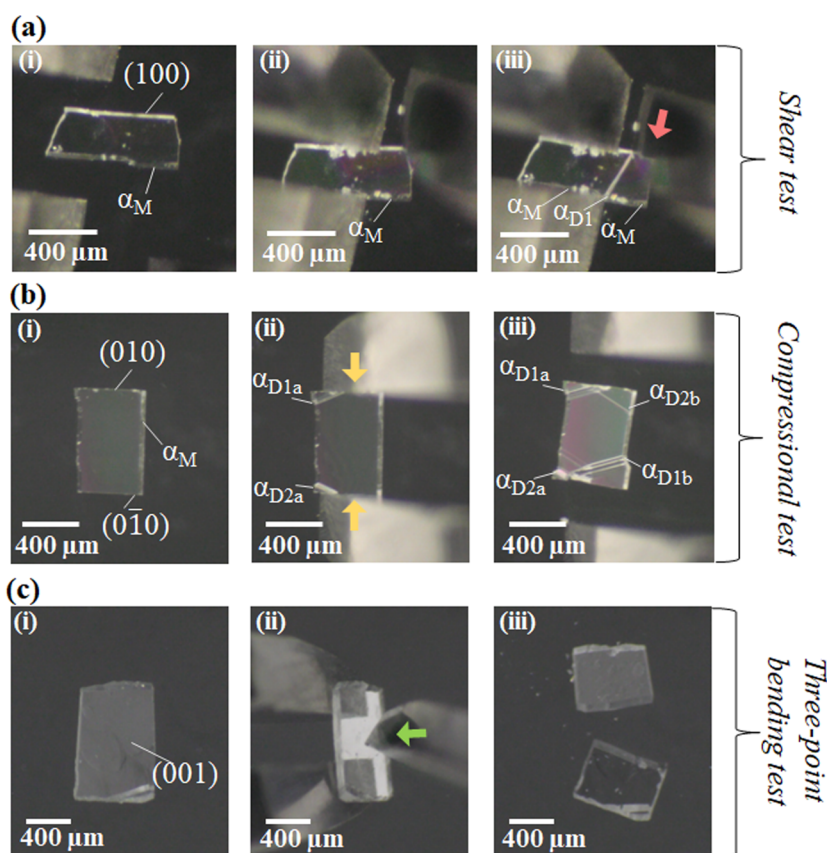
Figure 2. Snapshots of deformation by (a) shear stress, (b) compressional stress, and (c) three-point bending test on the respective planes of crystal **1**.
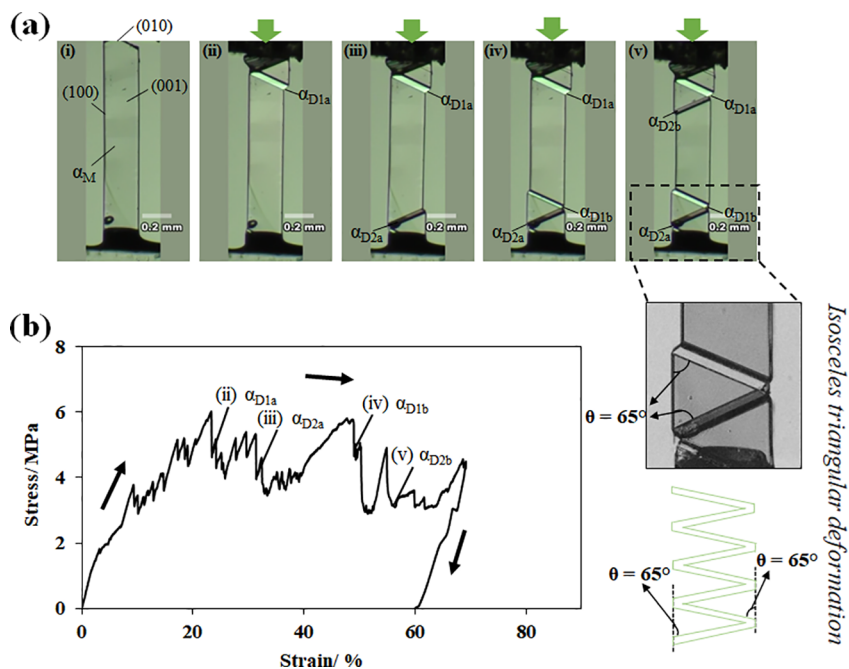

Figure 3. (a) Snapshots of deformed crystal upon application of compression test on the crystal face $(010/0\overline{1}0)$ and (b) the corresponding stress-displacement curve. The critical coercive stress of the daughter domains (α_{D1a}, α_{D2a}, α_{D1b}, α_{D2b}) in the crystal upon compression stress is depicted by parts ii, iii, iv, and v, respectively, in the stress-displacement curve.

Two-Directional Ferroelastic Deformation. The deformation behavior of the single crystal of **1** was tested on the three faces of the crystal (100), (010), and (001) through a shear stress test, compression test, and three-point bending test,

respectively (Figure 1b). Distinct deformation behavior could be noticed through the application of shear stress or compressional stress or a three-point bending test (Figure 2; Movies S1, S2, and S3, SI). The schematic illustration of the crystal **1** with its
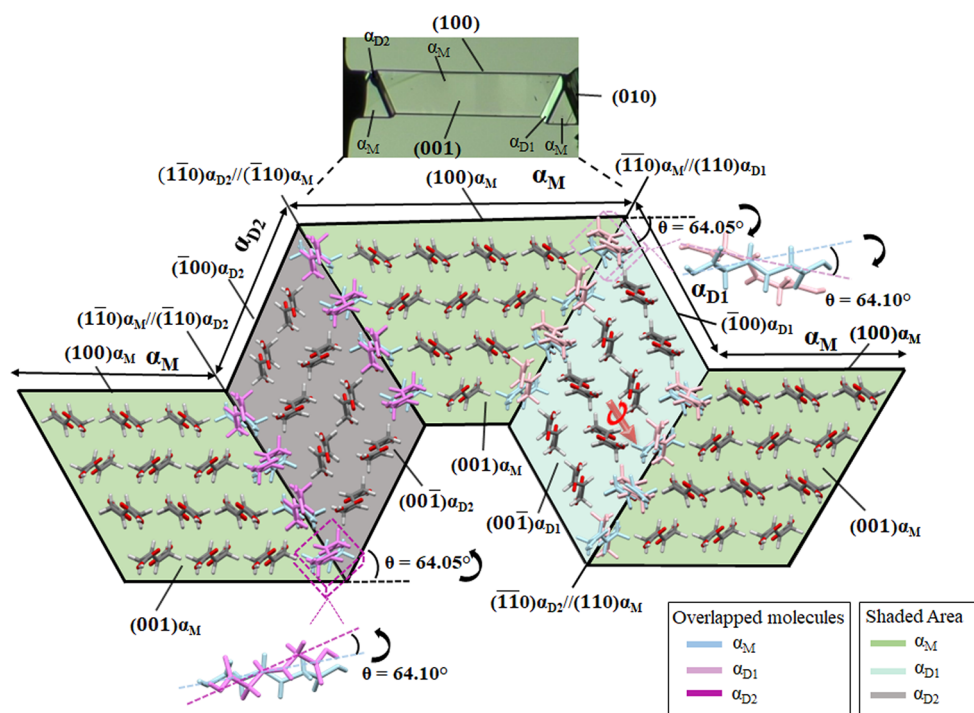
Figure 4. Estimated connecting manners of the parent (α_M) and daughter domains (α_{D1} and α_{D2}). Molecules at the interface in the α_M and α_{D1} domains and α_{D2} are colored in light blue, pink, and purple, respectively.

face indexes and the corresponding deformation behavior of the single crystal of **1** upon each deformation test are illustrated in Figures 1b and 2. The single crystal of **1** exhibited one-directional ferroelastic deformation when shear stress was applied on the $(100/\bar{1}00)$ plane by tweezers as detected by a polarized microscope (Figure 2a; Movie S1, SI). However, two-directional ferroelastic deformation was observed when compressional stress was applied on the $(010/0\bar{1}0)$ plane simultaneously (Figure 2b; Movie S2, SI). The two-directional ferroelastic deformation was accompanied by stress-induced formation of daughter domains (α_{D1} and α_{D2}) from the initial crystal phase (α_M form) with a clear phase boundary line at a bending angle of 65° clockwise in the α_{D1} case as shown in Figure 2b. The same bending angle was observed in the α_{D2} case but in the counterclockwise direction. In contrast, the crystal exhibited a brittle nature during the three-point bending test by tweezers when stress was applied on the (001) plane (Figure 2c; Movie S3, SI).

The two-directional ferroelastic deformation was further analyzed by measuring the stress-displacement curve. With the increasing compressive stress on the $(010/0\bar{1}0)$ plane, a two-directional ferroelastic deformation was initiated. The nucleation and growth of daughter domains (α_{D1a}, α_{D2a}) were observed at coercive stresses averaging 4.6 and 4.5 MPa, respectively (Figure 3; Movie S4, SI). Further, the appearance of the daughter domains (α_{D1b}, α_{D2b}) was observed at coercive stresses averaging 3.9 and 3.85 MPa, respectively (Figure 3). Interestingly, the pair of daughter domains (α_{D1a} and α_{D2b}, α_{D1b} and α_{D2a}) at either end exhibited a bending angle of 65°, making an isosceles triangle by the two daughter domains. This resulted in consecutive isosceles triangle-shaped daughter domains resembling a unique scissor-like movement in this two-directional ferroelastic deformation. The reversal of deformation by extension could not be recorded because the shear force was less effective than the tensile force. The critical

shear stress was almost identical, independent of the interfacial directional differences in ferroelastic deformation. To the best of our knowledge, this is the first example of two-directional ferroelastic deformation in organic crystals generated through a compression test. In addition, the obtained higher forward shear stress was approximately 7 times higher than our first report of ferroelastic organic crystal 5-chloro-2-nitroaniline[14] and other organoferroelastic crystals.

Furthermore, the stress-displacement graph was recorded by the application of a shear test. With increasing the shear stress on the (100) and $(\bar{1}00)$ planes of the single crystal of **1**, it deformed with the formation of stress-induced daughter domains, α_{D1} and α_{D2}, from the mother domain (α_M) at critical shear stresses of 0.7 and 0.75 MPa, respectively at RT (Figure S2, Movie S5, SI). The stress–strain curves showed a forward typical plateau corresponding to the propagation of the stress-induced daughter forms in the ferroelastic deformation (Figure S2). On removal of the stress, spontaneous strain was developed. As a result, the crystal could not be returned to its original shape, depicting a ferroelastic deformation.

Eventually, a three-point bending test on a universal testing instrument was used to determine the mechanical strength by measuring the elastic modulus of the crystal (Figure S3, SI).[7,40,41] The single crystal was subjected to a 14 MPa stress on the face $(001/00\bar{1})$ in the three-point bending test at RT (Figure S3, Movie S6, SI). The elastic modulus was calculated from the slope of the stress–strain curve of the single crystal (data conversion based on eq S1 and S2, SI). With the increase of stress on the face $(001/00\bar{1})$, the crystal was sustained until the stress of 14 MPa. In contrast to the (100/010) plane, the crystal exhibited elastic behavior, followed by breaking beyond the yield point on applying stress. The elastic modulus of crystal **1** was determined in the range of 1.7−3.23 GPa (Table S1). The different mechanical behavior on different planes is clearly due to the anisotropic interactions in the organic crystal.
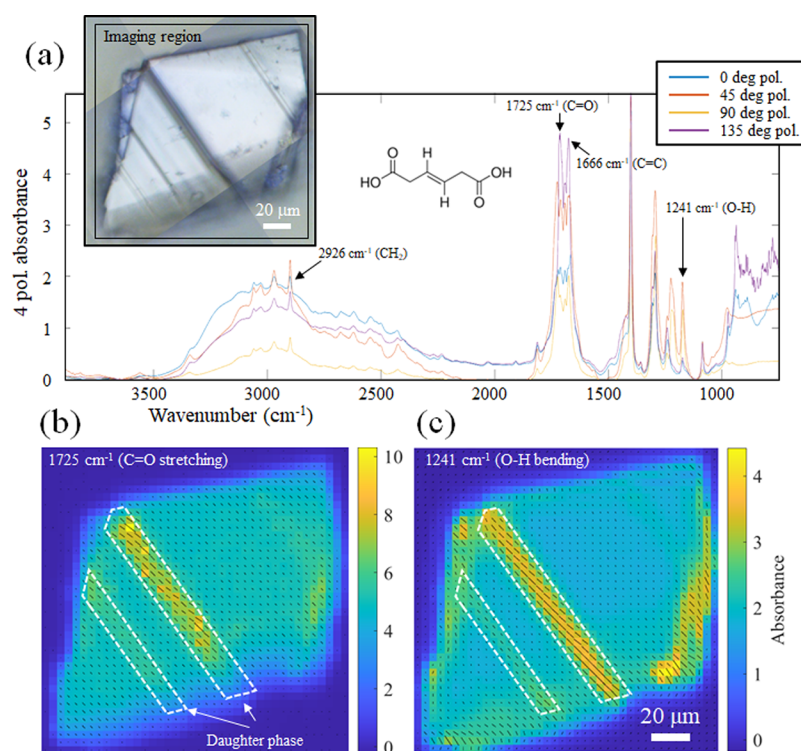
Figure 5. Results obtained from the four-angle polarization approach based on synchrotron-FTIR microspectroscopic data, indicating differences in the molecular orientation of mother and daughter phases. (a) A comparison of polarized synchrotron-FTIR spectra collected from the same location on the crystal using four angles of polarization (i.e., $\theta = 0°$, $45°$, $90°$, and $135°$). The key absorption peaks were labeled and assigned to specific vibrational modes. Inset: The optical image of crystal **1** under a visible microscope. (b, c) The vector maps show the orientation distribution of the $\nu(C=O)$ stretching and $\delta(O-H)$ bending transition dipole moment from left to right, respectively. The regions of the daughter phase are indicated with the dashed line in b and c. The background image of the vector map is the average absorbance of all four polarized images, which corresponds to the nonpolar image of the absorbance.

Crystallographic Studies. In order to unravel the structural mechanism responsible for the compressive induced two-directional ferroelasticity in crystal **1**, a detailed structural investigation by crystallographic studies and energy framework analysis was executed (Figures 4 and 7; Figures S10−S12, SI). Crystal **1** crystallizes in the monoclinic system with the $P2_1/n$ space group at RT, hereby referred to as the initial mother form (α_M; Table S2, SI). The crystal structure was similar to the previously reported one.[42] Single-crystal XRD analyses of the bent crystal of **1** revealed that the deformation is caused by mechanical twinning, which can be observed in the reciprocal lattices system (Figure S4, SI). The daughter domains formed at the upper and lower ends of the crystal are described as the first daughter α_{D1} and second daughter α_{D2}, respectively (Figure 4). According to crystal structure analyses and face indexing of the twinned crystal, the two-directional ferroelasticity is based on 180° rotational mechanical twinning attributed to the molecular movement (Figure S5, SI). Upon application of compressional force on the $(010/0\bar{1}0)$ plane, the crystal bent by 64.05° by pushing the (100) α_M face along the $(\bar{1}\bar{1}0)\alpha_M$ plane with the conversion of the α_M domain into an α_{D1} domain via reorientation of crystal **1**. In this deformation, a 64.10° tilt along its acidic moiety resembling a clockwise molecular movement in the 2D sheet was observed (Figure 4). However, the α_{D2} formation proceeded exactly in an opposite manner. The crystal also bent by 64.05° but by pushing the reverse plane instead of the former, i.e., the $(\bar{1}00)$ α_M face along the $(1\bar{1}0)\alpha_M$ plane on the application of the compressional stress on the crystal face $(0\bar{1}0/010)$ or excess compressional stress on the

$(010/0\bar{1}0)$ plane. The conversion of the α_M domain into the α_{D2} domain was also the same via reorientation, i.e., 64.10° tilts along its acidic moiety, but it resembles a counterclockwise movement in the 2D sheet (Figure 4). The twin domains of α_M, α_{D1} and α_{D2}, are related by a 180° rotation about the twin axis that is perpendicular to the twin interface of $(\bar{1}\bar{1}0)\alpha_M//$ $(110)\alpha_{D1}$ and $(1\bar{1}0)\alpha_M//(\bar{1}10)\alpha_{D2}$, respectively. The similar deformation and molecular movement about these twin axes imply that the two faces are crystallographically equivalent in the present monoclinic system. Based on the crystallographic analysis, a bending angle of 64.10° between α_M and twin domains (α_{D1} and α_{D2} in clockwise and counterclockwise manner) at their respective twin interfaces $(\bar{1}\bar{1}0)\alpha_M//(110)\alpha_{D1}$ and $(1\bar{1}0)\alpha_M//(\bar{1}10)\alpha_{D2}$ could be anticipated. This is corroborated with the 65° bending angle observed by optical microscopy (Figure 3b).

The differences in C—C bond lengths between C1—C2 (1.498 Å), C2—C3 (1.491 Å), and C3—C3 (1.312 Å) in C atom catenation indicate that C1—C2 and C2—C3 are single bonded and C3—C3 is double bonded ethylene C atoms, as inferred by the half-molecule in the asymmetric unit. The twisting of the carboxylic acid groups may have facilitated the deformation of the entire molecule, leading to a severe twist of the carbon chain resulting in the zigzag chain shape of the crystal (**1**). These acid groups also helped to stabilize the structure by generating eight-membered cyclic dimers with the R_2^2 (8) graph-set motif. The lateral molecules are connected end-to-end by the carboxy dimer motifs, creating an endless chain of hydrogen bonds along the c axis. In the crystal of **1**, infinite

strong H-bonded 1D tapes are formed via two strong and equivalent intermolecular O—H⋯O interactions (2.67 Å, 177.78°) along the [001] direction. However, along the compressional direction, intermolecular sheets interacted via two evenly balanced and weak C—H⋯O interactions (3.334 Å/ 122.02° and 3.34 Å/114.96°) in a side-to-end manner (Figure S6, SI). The overall crystal structure was similar to the two-dimension side to end synthons satisfying the required criteria to obtain more than one-dimensional bending, as mentioned by Saha and Desiraju.[26] They emphasized that the herringbone arrangement could be a prerequisite for accomplishing more than one-dimensional bending. However, this two-directional ferroelastic deformation differs from our previously reported two-dimensional ferroelastic deformation in two mutually orthogonal planes in 4-iodoanlinine crystals. In this two-directional ferroelastic deformation of crystals of **1**, similar daughter domains with the same bending resembling a scissor like movement were generated on application of simultaneous stress on opposite planes. In contrast, distinct daughter domains were generated with different bending angles in the two-dimensional ferroelastic deformation of 4-iodoanlinine. As a result, the prerequisite structural conditions hold true for this case also.

Structural Analysis by Polarized Synchrotron-FTIR Microspectroscopy. The spatial distribution of the molecular structure in the crystal was also analyzed under phase transition (deformation) by polarized synchrotron-FTIR microspectroscopy in transmission mode, using four-angle polarization (4-pol) setup similar to our previous studies.[43−46] The superior characteristics of high photon flux and diffraction-limited spatial resolution achieved by synchrotron-FTIR microspectroscopy allowed molecular characterization of the single crystal to be mapped and visualized at a high spatial resolution directly on the mother and daughter domains in the (001) plane using a 5 μm × 5 μm pixel size without interrupting the crystal. The imaging with four angle polarization is sensitive to the in-plane orientation of the transition dipole moment (TDM). The orientation of TDM in a molecule is related to the orientation of the entire molecule, so that the method can estimate the reorientation of the molecule from IR spectrum change. The change in the orientation of the TDM upon deformation was utilized to illustrate and compare the molecular level changes in the crystal domain. In particular, the orientation of the ν(C=O) stretching band at 1725 cm^{-1} and δ(O—H) bending at 1241 cm^{-1} were monitored. It is worth noting that the orientation TDM of the daughter domain O—H changes with respect to the mother domain. This change can be expected because of molecular movement of the twinned daughter domain with respect to the parent mother domain by a 64.10° tilt along its acidic moiety in the crystal structure. The orientation function of each TDM (f_{TDM}) obtained from the mother and daughter domain ν(C=O) stretching and δ(O—H) bending bands, respectively, were distinct (Figure 5) as a length and the direction of the f_{TDM} vector. Additionally, the orientation function of the dipole moment of ν(C=C) stretching band detected at 1666 cm^{-1} changes to a lesser extent than the ν(C=O) stretching and δ(O—H) bending band (Figure S7). This significant deviation of the TDM orientation in the mother and daughter domain confirms the reorientation of crystal **1** molecules and transformation in the two-directional ferroelastic deformation.

Investigation of the Anisotropic Thermophysical Properties. The thermal diffusivity of the single crystal was

measured by means of μ-TWA. The sensor and heater were attached on opposite faces of a single crystal to determine the thermal diffusivity along three axes of the crystal. Figure 6 shows
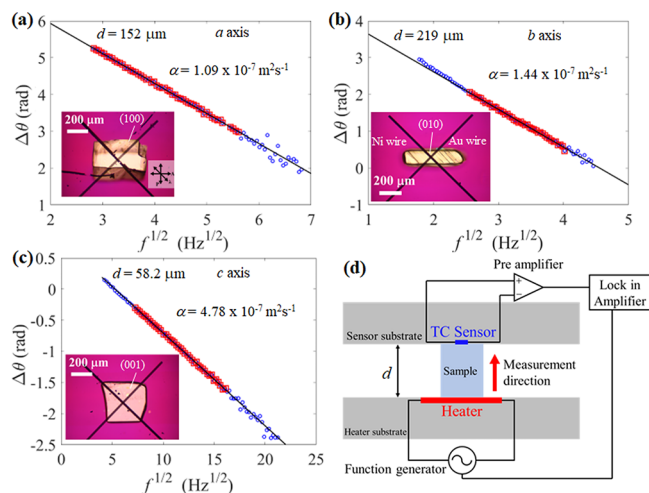

Figure 6. Frequency dependence of the phase delay measured for (a) sample 2 along the *a* axis, (b) sample 5 along the *b* axis, and (c) sample 8 along the *c* axis by μ-TWA, further details in Figure S8 and Table S3. The inset shows the optical image of each sample under the crossed polarized microscope (top view). A TC-type microsensor (20 μm × 20 μm) was attached on each face of the single crystal. The heater (0.25 × 1 mm) is made of ITO thin film so that it is not visible in the pictures. (d) Cross-sectional schematic view of the experimental system. The periodic heating and detection of the periodic temperature response from the sample were determined by the synchronized function generator and the lock-in amplifier.

the measured frequency dependence of the phase delay of the temperature wave for different directions in the sample. A high-frequency approximation was applied to the measured data, and the thermal diffusivity was estimated from the slope in the high frequency region. Measurements were performed for several samples for each crystal axis, and the average value for each crystal axis was used for the analysis. The determination of the thermal diffusivity from the phase delay is robust, as it is less affected by the thermal contact conductance (TCC) between the sensor, heater, and sample surface. As a result, the error is less than the standard deviation of the analysis. The measured thermal diffusivities are listed in Figure S8 and Table S3 together with the effective distance between the sensor and heater. The measured thermal diffusivity is not dependent on the distance/ length, confirming that the measurement is also independent of the system dimensionality, and the effect of TCC is minor. The measured averaged thermal diffusivities are highly anisotropic and were 1.04, 1.38, and 4.46 × 10^{-7} m^2 s^{-1} for the direction along the *a*, *b*, and *c* axes, respectively. It implies that crystal **1** transmits heat more effectively along the *c*-axis than on the other axis. This highly anisotropic thermal diffusivity was seen due to the anisotropic nature/intermolecular interaction of single crystals of **1**, which could be helpful in designing the efficient thermal management in microlevel miniaturization devices. The error range shown in the table is a 95% confidential region of each linear fit. The average of the range is less than 3%.

Furthermore, the thermal diffusivity values of the daughter domains of the crystal were examined: α_{D1} (4.68 × 10^{-7} m^{2}s^{-1}) and α_{D2} (3.61 × 10^{-7} m^2 s^{-1}) along the [00$\bar{1}$] directions (Figure S9, Table S4, SI). The thermal diffusivity values of the mother
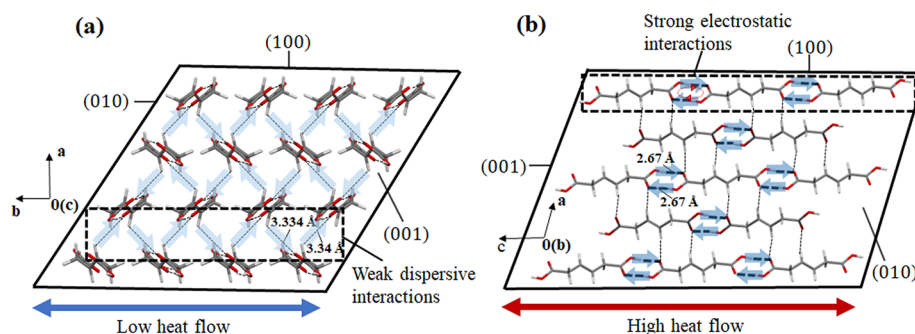
Figure 7. Crystal packing. (a) Crystal packing with its weak interactions along the *b* axis with side-to-end synthons, and (b) crystal packing with strong cyclic H interactions along the *c* axis. Blue and red arrows depict the heat flow directions as low and high, respectively.

and daughter domains were comparable and were within the range of experimental errors. The detailed values and errors of the measurements of the daughter domains of the crystal are presented in Table S4. These results could be attributed to the molecular movement via rotational mechanical twinning, where molecules are reoriented in the plane perpendicular to the direction of thermal diffusivity measurement.

Correlation of Anisotropic Structural Arrangement with Thermal Diffusivity and Mechanical Behavior. Overall, two crystallographically equivalent faces and the herringbone arrangement could be the reason behind the two directional ferroelasticity in the crystal of **1** during compressional stress on the $(010/0\overline{1}0)$ plane. The weak C—H⋯O interactions in the crystal structure could be held accountable for increased forward stress in the single crystal, which is in agreement with our previous findings that weak dispersive interactions facilitated the superelastic−ferroelastic interconversion shape memory cocrystal with an increased forward stress value.[17]

To unveil the relationship between the different thermal diffusivity values along with distinct mechanical deformation with crystal structure anisotropy, the interaction strengths and percentages on all three axes were investigated (Figure 7; Figures S10, S11, and S12, SI). The strong O−H⋯O interactions along the *c* axis could reduce the desired mechanical softness, thereby leading to a brittle nature in this direction. Strong cyclic H interactions constrain the molecular movement, and as a result, the crystal undergoes elastic behavior followed by breaking beyond the yield point with the application of stress on the face $(001/00\overline{1})$ in the three-point bending experiment. On the other hand, molecules are arranged via weak C−H⋯O interactions in a side-to-end manner along the *b* axis, which provides the space for molecular movement in the direction of two crystallographically equivalent faces. As a result, two-directional ferroelasticity was observed during compressional stress on the face $(010/0\overline{1}0)$. On the other hand, one directional ferroelastic deformation on the application of the shear test on the face $(100/\overline{1}00)$ was evident owing to the presence of weak C−H⋯O interactions along the *a* axis and the application of shear stress at only one crystallographically equivalent face.

The obtained interaction of the O−H by the crystal explorer software was the highest, which is 51.9%, whereas the C−H and C−O interactions were found at 9.5% and 3.0%, respectively (Figure S10, SI). Additionally, the molecules strongly interacted via electrostatically dominated O—H⋯O hydrogen bonds with a total aggregate interaction energy of -69.1 kJ mol^{-1} along the *c* axis (Figures S11 and S12c, SI). It could be the reason for the highest thermal diffusivity along the *c* axis, where the robust,

strong, and electrostatically dominated O—H⋯O hydrogen bonds determine the thermal diffusivity value. The stronger hydrogen bond has a shorter intermolecular distance, which could lead to increased interatomic forces across the intermolecular interface, and thus higher thermal diffusivity was perceived. Stronger intermolecular interaction and shorter molecular distance along the *c* axis increase the mean free path (MFP) and group velocity of phonons along this direction and increase the time constant of the structural relaxation process. Such an increase of thermal diffusivity or thermal conductivity was also reported and interpreted in the case of the liquid crystal (LC). In the case of LC having a dipole interaction along a specific direction, the increase in thermal diffusivity was observed, and from the molecular dynamics simulation, the effective increase in thermal diffusivity due to the dipole−dipole interaction was about 0.1 W/m/K.[47] In contrast, dispersion dominated C−H⋯O interactions along the *a/b* axis can provide the molecular movement and absorb/keep the mechanical strain due to weak and longer intermolecular distances with total aggregate interaction energy -12.8 and -11.2 kJ mol^{-1} (Figures S11 and S12c, SI). Thereby, the lowest thermal diffusivity was observed in this direction, and high molecular movement was like two-directional ferroelasticity. The contrast in molecular aggregate interaction energy strongly affects the total thermal diffusivity, so the aggregation state of the molecule plays an important role even in the case of heat diffusion in a molecular base material.

■ CONCLUSIONS

This study depicts the first example of a two-directional ferroelastic deformation in organic crystals of *trans*-3-hexane-dioic acid by the application of compressive stress. The distinct deformation behavior on the three faces of the crystal was clearly illustrated by various force measurement techniques, namely, shear stress, compression test, and three-point bending test. On application of compressive stress on $(010/0\overline{1}0)$, two-directional ferroelastic deformation with a unique scissor-like movement reflected by the appearance of two daughter domains generated from the initial mother domain was observed. The underlying mechanism was elucidated by comprehensive crystallographic studies and was attributed to mechanical twinning. The presence of two crystallographically equivalent faces and the herringbone arrangement could be the reason for the detection of two-directional ferroelasticity during the compressional stress on the $(010/0\overline{1}0)$ plane. In addition, a relationship between the thermal diffusivity values, mechanical deformations, and the anisotropic interactions along the three axes were confirmed. O—H⋯O interactions with a shorter intermolecular distance

manifested higher thermal diffusivity. In contrast, relatively weak C−H···O interactions resulted in low thermal diffusivity while the side-to-end arrangement with weak C−H···O interactions contributed to the two-directional ferroelasticity. The structural mechanism indicated in this study would be insightful not only for the design and development of flexible organic molecular crystals but also for thermally controllable material under the mechanical stress.

■ MATERIALS AND METHODS

Materials. *trans*-3-Hexenedioic acid (**1**) was procured from Tokyo Chemical Industry Co., Ltd. and was used without being purified further.

Preparation of Single Crystals. Block-shaped single crystals of **1** were obtained from a methanol solution of *trans*-3-hexenedioic acid with a slow evaporation technique.

Microscopic Observation. The mechanical deformation of crystals was carried out by tweezers and was recorded using an optical microscope (SZ61, Olympus Co.) with built-in polarizing plates and a digital camera.

Force Measurements. *Shear Test.* The shear test at room temperature was conducted by using a universal testing machine. A crystal was bonded to a glass base and then sheared using a glass jig attached to a load cell at a displacement rate of 3 μm s^{-1} on the crystal face $(100/\overline{1}00)$, and the deformation behavior was observed using a polarized light microscope.

Compressional Test. The compression test was performed by using a universal testing machine. A crystal was fixed to a glass base and then compressed using a flat glass metallic jig attached to a load cell at a displacement rate of 3 μm s^{-1} on the crystal face $(010/0\overline{1}0)$, and the deformation behavior was observed using a polarized light microscope.

Three-Point Bending Test. The three-point bending test experiment was accomplished using a universal testing machine coupled with a polarized light microscope. A single crystal was put on two-point support, and a metal-blade jig was used to apply stress to the crystal (Figure S3). At a displacement rate of 3 μm s^{-1}, the jig was pushed on the crystal face $(001/00\overline{1})$ downward (press). The sharp breaking point was detected after the elastic limit, and the deformation behavior was observed by using a polarized light microscope. Further calculation details are mentioned in the Supporting Information.

Single-Crystal X-ray Structure Analysis. Single-crystal X-ray diffraction (SCXRD) data of the parent (α_M) and deformed daughters (α_{D1} and α_{D2}) of the obtained **1** single crystal were collected and solved based on diffraction patterns on a Bruker D8 VENTURE (PHOTON III 14) using graphite monochromated Mo Kα radiation ($\lambda = 0.71073$ Å) at room temperature (rt). Intrinsic phasing methods (SHELXT)[48] were used to solve the structure, and full-matrix least-squares calculations on F^2 (SHELXL)[49] were used to refine it. A Bruker APEX3 (2019) was used to index the facets of the parent and twinned domains based on the obtained data. Cell Now (Sheldrick, 2008) was used to examine the orientational link between the parent and twinned domains. Non-hydrogen atoms were refined anisotropically, while hydrogen atoms were fixed at calculated positions using a riding model approximation. Mercury CSD was used to measure Miller plane interplanar angles.

Hirshfeld Surface Analysis. The Hirshfeld surface study of the single crystal of **1** was conducted using the CrystalExplorer 21.5 package based on the crystal geometry. CrystalExplorer 21.5 was used to generate 2D fingerprint plots and energy frameworks.

Thermal Analysis. Differential scanning calorimetry (DSC) and thermogravimetric analysis (TGA) profiles of **1** crystal were measured on DSC-60 and DTG-60 instruments (Shimadzu Co.), respectively. For the DSC and TGA analyses, about 5 mg of the sample was heated to a temperature range of 25−250 °C and 25−400 °C at a heating rate of 5 °C min^{-1} under a nitrogen gas flow (50 mL min^{-1}).

Thermal Diffusivity Analysis. The directional thermal diffusivity of the single crystal of **1** was measured by the μ-TWA method. The single crystal having a size of approximately 100 μm × 100 μm × 100 μm (thickness) was sandwiched between a micro heater (1 mm × 250 μm) and a micro thermocouple (TC) type sensor (20 μm × 20 μm). The periodic Joule heating was applied from the heater and detected by the micro-TC heater. The detailed configuration of the measurement can be found in previous work.[50] The detected signal was analyzed based on the principle of temperature wave propagation. Especially, the thermal diffusivity was estimated from its phase delay between the heater and sensor surfaces. The phase delay of the periodic temperature response can be written as follows.

$$\Delta \theta = -\sigma + \tan^{-1}\left\{ \frac{-(1-b)^2 \exp(-2\sigma) \sin 2\sigma}{(1+b)^2 - (1-b)^2 \exp(-2\sigma) \cos 2\sigma} \right\} - \frac{\pi}{4}$$

$$\sigma = \sqrt{\frac{\pi f}{\alpha}}\, d,$$

$$b = \frac{e_s}{e}$$

Here, α is the thermal diffusivity along the thickness direction, d is the thickness of the sample, f is the frequency of the applied temperature wave, e is the thermal effusivity of the sample, and e_s is the thermal effusivity of the substrate. At sufficiently high frequency ($\sigma \gg 1$), the first term of the equation becomes dominant, and frequency dependence of the phase delay data can be analyzed by a linear function with the slope correlated to the thermal diffusivity along the thickness direction. The frequency of temperature wave was typically set between the 10 Hz to 10 kHz range for the measurement of frequency dependence of the phase delay.

Polarized Synchrotron-FTIR Microspectroscopy. The synchrotron-FTIR measurement was performed on the Infrared Microspectroscopy (IRM) Beamline at the Australian Synchrotron (Victoria, Australia), using a Bruker Vertex 80v spectrometer coupled with a Hyperion 3000 FTIR microscope and a liquid-nitrogen-cooled narrow-band mercury cadmium telluride (MCT) detector (Bruker Optik GmbH, Ettlingen, Germany). The mapping measurement was performed on the single crystal, which was placed onto a clean BaF$_2$ window, in transmission mode using an identical pair of 36× objectives and condensers (NA = 0.50), a projected aperture of 5.6 μm in diameter, and eight coadded scans per spectrum. Background spectra were acquired on the clean surface of the same BaF$_2$ window using 128 coadded scans. The polarizer used in this study was a wire-grid KRS-5 (Pike Technologies Inc., Madison, WI). All of the synchrotron-FTIR spectra were recorded within a spectral range of 3800−700 cm^{-1} using 4 cm^{-1} spectral resolution. Blackman-Harris 3-Term apodization, Mertz phase correction, and a zero-filling factor of 2 were set as default acquisition parameters using the OPUS 8 software suite (Bruker Optik GmbH, Ettlingen, Germany).

■ ASSOCIATED CONTENT

ⓈI Supporting Information

The Supporting Information is available free of charge at https://pubs.acs.org/doi/10.1021/jacs.3c05545.

Movie S1. Shear stress based mechanical deformation $\alpha_M \rightarrow \alpha_{D1}$ transformations by tweezers on $(100/\overline{1}00)$ plane (MPG)

Movie S2. Compressional stress based mechanical deformation $\alpha_M \rightarrow \alpha_{D1}$ and α_{D2} transformations by tweezers on $(010/0\overline{1}0)$ plane (MPG)

Movie S3. Three-point bending test by tweezers on $(001/00\overline{1})$ plane (MPG)

Movie S4. Compression stress-displacement test on $(010/0\overline{1}0)$ plane at room temperature (MPG)

Movie S5. Shear stress-displacement test on $(100/\overline{1}00)$ plane at room temperature (MPG)

Movie S6. Three-point bending test on $(001/00\overline{1})$ plane at room temperature (MPG)

Detailed information about thermal and crystallographic studies (PDF)

Accession Codes

CCDC 2264409−2264411 contain the supplementary crystallographic data for this paper. These data can be obtained free of charge via www.ccdc.cam.ac.uk/data_request/cif, or by emailing data_request@ccdc.cam.ac.uk, or by contacting The Cambridge Crystallographic Data Centre, 12 Union Road, Cambridge CB2 1EZ, UK; fax: +44 1223 336033.

■ AUTHOR INFORMATION

Corresponding Authors

Junko Morikawa − *School of Materials and Chemical Technology, Tokyo Institute of Technology, Tokyo 152-8550, Japan; International Research Frontiers Initiative (IRFI), Tokyo Institute of Technology, Yokohama, Kanagawa 226-8501, Japan;* orcid.org/0000-0002-9530-9478; Email: morikawa.j.aa@m.titech.ac.jp

Satoshi Takamizawa − *Department of Materials System Science, Graduate School of Nanobioscience, Yokohama City University, Yokohama, Kanagawa 236-0027, Japan;* orcid.org/0000-0002-6677-3781; Email: staka@yokohama-cu.ac.jp

Authors

Subham Ranjan − *Department of Materials System Science, Graduate School of Nanobioscience, Yokohama City University, Yokohama, Kanagawa 236-0027, Japan;* orcid.org/0000-0003-3665-3292

Meguya Ryu − *National Metrology Institute of Japan (NMIJ), National Institute of Advanced Industrial Science and Technology (AIST), Tsukuba 305-8563, Japan*

Ryota Morioka − *School of Materials and Chemical Technology, Tokyo Institute of Technology, Tokyo 152-8550, Japan*

Shuji Kamegaki − *School of Materials and Chemical Technology, Tokyo Institute of Technology, Tokyo 152-8550, Japan*

Soon Hock Ng − *Optical Sciences Centre and ARC Training Centre in Surface Engineering for Advanced Materials (SEAM), School of Science, Swinburne University of Technology, Victoria 3122, Australia*

Daniel Smith − *Optical Sciences Centre and ARC Training Centre in Surface Engineering for Advanced Materials (SEAM), School of Science, Swinburne University of Technology, Victoria 3122, Australia*

Jitraporn Vongsvivut − *Infrared Microspectroscopy (IRM) Beamline, ANSTO—Australian Synchrotron, Clayton, Victoria 3168, Australia*

Mark J. Tobin − *Infrared Microspectroscopy (IRM) Beamline, ANSTO—Australian Synchrotron, Clayton, Victoria 3168, Australia*

Saulius Juodkazis − *Optical Sciences Centre and ARC Training Centre in Surface Engineering for Advanced Materials (SEAM), School of Science, Swinburne University of Technology, Victoria 3122, Australia; International Research Frontiers Initiative (IRFI), Tokyo Institute of Technology, Yokohama, Kanagawa 226-8501, Japan;* orcid.org/0000-0003-3542-3874

Complete contact information is available at:
https://pubs.acs.org/10.1021/jacs.3c05545

Notes

The authors declare no competing financial interest.

■ ACKNOWLEDGMENTS

■ REFERENCES

(1) Reddy, C. M.; Gundakaram, R. C.; Basavoju, S.; Kirchner, M. T.; Padmanabhan, K. A.; Desiraju, G. R. Structural basis for bending of organic crystals. *Chem. Commun.* **2005**, 3945−3947.

(2) Lu, Z.; Zhang, Y.; Liu, H.; Ye, K.; Liu, W.; Zhang, H. Optical waveguiding organic single crystals exhibiting physical and chemical bending features. *Angew. Chem., Int. Ed.* **2020**, *59*, 4299−4303.

(3) Takazawa, K.; Inoue, J.-i.; Mitsuishi, K.; Yoshida, Y.; Kishida, H.; Tinnemans, P.; Engelkamp, H.; Christianen, P. C. Phase-transition-induced jumping, bending, and wriggling of single crystal nanofibers of coronene. *Sci. Rep.* **2021**, *11*, 3175.

(4) Gupta, P.; Panda, T.; Allu, S.; Borah, S.; Baishya, A.; Gunnam, A.; Nangia, A.; Naumov, P.; Nath, N. K. Crystalline acylhydrazone photoswitches with multiple mechanical responses. *Cryst. Growth Des.* **2019**, *19*, 3039−3044.

(5) Lun, M.-M.; Zhang, T.; Su, C.-Y.; Li, J.; Zhang, Z.-X.; Fu, D.-W.; Lu, H.-F. A ferroelastic molecular rotator [(Me$_2$N(CH$_2$)$_2$NH$_3$)(18-crown-6)] triflate with dual dielectric switches. *Mater. Chem. Front.* **2022**, *6*, 1929−1937.

(6) Wang, K.; Mishra, M. K.; Sun, C. C. Exceptionally elastic single-component pharmaceutical crystals. *Chem. Mater.* **2019**, *31* (5), 1794−1799.

(7) Worthy, A.; Grosjean, A.; Pfrunder, M. C.; Xu, Y.; Yan, C.; Edwards, G.; Clegg, J. K.; McMurtrie, J. C. Atomic resolution of structural changes in elastic crystals of copper (II) acetylacetonate. *Nat. Chem.* **2018**, *10*, 65−69.

(8) Thompson, A. J.; Chamorro Orue, A. I.; Nair, A. J.; Price, J. R.; McMurtrie, J.; Clegg, J. K. Elastically flexible molecular crystals. *Chem. Soc. Rev.* **2021**, *50*, 11725−11740.

(9) Chattoraj, S.; Shi, L.; Sun, C. C. Understanding the relationship between crystal structure, plasticity and compaction behaviour of theophylline, methyl gallate, and their 1:1 co-crystal. *CrystEngComm* **2010**, *12*, 2466−2472.

(10) Mondal, A.; Bhattacharya, B.; Das, S.; Bhunia, S.; Chowdhury, R.; Dey, S.; Reddy, C. M. Metal-like Ductility in Organic Plastic Crystals: Role of Molecular Shape and Dihydrogen Bonding Interactions in Aminoboranes. *Angew. Chem., Int. Ed.* **2020**, *59*, 10971−10980.

(11) Krishna, G. R.; Devarapalli, R.; Lal, G.; Reddy, C. M. Mechanically flexible organic crystals achieved by introducing weak interactions in structure: supramolecular shape synthons. *J. Am. Chem. Soc.* **2016**, *138*, 13561−13567.

(12) Hasija, A.; Thompson, A. J.; Singh, L.; S. N., M.; Mangalampalli, K. S. R. N.; McMurtrie, J. C.; Bhattacharjee, M.; Clegg, J. K.; Chopra, D. Plastic Deformation in a Molecular Crystal Enables a Piezoresistive Response. *Small* **2023**, *19*, 2206169.

(13) Takamizawa, S.; Miyamoto, Y. Superelastic organic crystals. *Angew. Chem., Int. Ed.* **2014**, *126*, 7090−7093.

(14) Takamizawa, S.; Takasaki, Y. Superelastic Shape Recovery of Mechanically Twinned 3, 5-Difluorobenzoic Acid Crystals. *Angew. Chem., Int. Ed.* **2015**, *127*, 4897−4899.

(15) Sasaki, T.; Sakamoto, S.; Takasaki, Y.; Takamizawa, S. A Multidirectional Superelastic Organic Crystal by Versatile Ferroelastical Manipulation. *Angew. Chem., Int. Ed.* **2020**, *132*, 4370−4373.

(16) Li, Y. X.; Liu, Z. K.; Cao, J.; Tao, J.; Yao, Z. S. Stress-Induced Inversion of Linear Dichroism by 4, 4′-Bipyridine Rotation in a Superelastic Organic Single Crystal. *Angew. Chem., Int. Ed.* **2023**, *62*, No. e202217977.

(17) Mir, S. H.; Takasaki, Y.; Engel, E. R.; Takamizawa, S. Ferroelasticity in an organic crystal: a macroscopic and molecular level study. *Angew. Chem., Int. Ed.* **2017**, *56*, 15882−15885.

(18) Engel, E. R.; Takamizawa, S. Versatile ferroelastic deformability in an organic single crystal by twinning about a molecular zone axis. *Angew. Chem., Int. Ed.* **2018**, *57*, 11888−11892.

(19) Moskwa, M.; Ganczar, E.; Sobieszczyk, P.; Medycki, W.; Zieliński, P.; Jakubas, R.; Bator, G. y. Temperature-Stimulus Responsive Ferroelastic Molecular-Ionic Crystal:$(C_8H_{20}N)[BF_4]$. *J. Phys. Chem. C* **2020**, *124*, 18209−18218.

(20) Park, S. K.; Sun, H.; Chung, H.; Patel, B. B.; Zhang, F.; Davies, D. W.; Woods, T. J.; Zhao, K.; Diao, Y. Super-and ferroelastic organic semiconductors for ultraflexible single-crystal electronics. *Angew. Chem., Int. Ed.* **2020**, *132*, 13104−13112.

(21) Takamizawa, S.; Takasaki, Y. Shape-memory effect in an organosuperelastic crystal. *Chem. Sci.* **2016**, *7*, 1527−1534.

(22) Ranjan, S.; Honda, H.; Takamizawa, S. Thermo-mechanical reversibility in a shape memory organic salt. *J. Mater. Chem. C* **2022**, *10*, 12765−12775.

(23) Mutai, T.; Sasaki, T.; Sakamoto, S.; Yoshikawa, I.; Houjou, H.; Takamizawa, S. A superelastochromic crystal. *Nat. Commun.* **2020**, *11*, 1824.

(24) Seki, T.; Feng, C.; Kashiyama, K.; Sakamoto, S.; Takasaki, Y.; Sasaki, T.; Takamizawa, S.; Ito, H. Photoluminescent ferroelastic molecular crystals. *Angew. Chem., Int. Ed.* **2020**, *59*, 8839−8843.

(25) Takamizawa, S.; Takasaki, Y.; Sasaki, T.; Ozaki, N. Super-plasticity in an organic crystal. *Nat. Commun.* **2018**, *9*, 3984.

(26) Saha, S.; Desiraju, G. R. Crystal engineering of hand-twisted helical crystals. *J. Am. Chem. Soc.* **2017**, *139*, 1975−1983.

(27) Awad, W. M.; Davies, D. W.; Kitagawa, D.; Mahmoud Halabi, J.; Al-Handawi, M. B.; Tahir, I.; Tong, F.; Campillo-Alvarado, G.; Shtukenberg, A. G.; Alkhidir, T.; Hagiwara, Y.; Almehairbi, M.; Lan, L.; Hasebe, S.; Karothu, D. P.; Mohamed, S.; Koshima, H.; Kobatake, S.; Diao, Y.; Chandrasekar, R.; Zhang, H.; Sun, C. C.; Bardeen, C.; Al-Kaysi, R. O.; Kahr, B.; Naumov, P. Mechanical properties and peculiarities of molecular crystals. *Chem. Soc. Rev.* **2023**, *52*, 3098−3169.

(28) Abrahams, S. Ferroelasticity. *Mater. Res. Bull.* **1971**, *6*, 881−890.

(29) Mir, S. H.; Takasaki, Y.; Engel, E. R.; Takamizawa, S. Enhancement of dissipated energy by large bending of an organic single crystal undergoing twinning deformation. *RSC Adv.* **2018**, *8*, 21933−21936.

(30) Sasaki, T.; Sakamoto, S.; Nishizawa, K.; Takamizawa, S. Ferroelasticity with a Biased Hysteresis Loop in a Co-Crystal of Pimelic Acid and 1, 2-Di (4-pyridyl) ethane. *Cryst. Growth Des.* **2020**, *20*, 3913−3917.

(31) Park, S. K.; Sun, H.; Bernhardt, M.; Hwang, K.; Anthony, J. E.; Zhao, K.; Diao, Y. Unraveling Molecular Design Principle of Ferroelasticity in Organic Semiconductor Crystals with Two-Dimensional Brickwork Packing. *Chem. Mater.* **2023**, *35* (1), 81−93.

(32) Sun, H.; Park, S. K.; Diao, Y.; Kvam, E. P.; Zhao, K. Molecular mechanisms of superelasticity and ferroelasticity in organic semiconductor crystals. *Chem. Mater.* **2021**, *33*, 1883−1892.

(33) Gao, P.; Britson, J.; Nelson, C. T.; Jokisaari, J. R.; Duan, C.; Trassin, M.; Baek, S.-H.; Guo, H.; Li, L.; Wang, Y.; Chu, Y.-H.; Minor, A. M.; Eom, C.-B.; Ramesh, R.; Chen, L.-Q.; Pan, X. Ferroelastic domain switching dynamics under electrical and mechanical excitations. *Nat. Commun.* **2014**, *5*, 3801.

(34) Röhm, H.; Leonhard, T.; Schulz, A. D.; Wagner, S.; Hoffmann, M. J.; Colsmann, A. Ferroelectric properties of perovskite thin films and their implications for solar energy conversion. *Adv. Mater.* **2019**, *31*, 1806661.

(35) Liao, W.-Q.; Zeng, Y.-L.; Tang, Y.-Y.; Peng, H.; Liu, J.-C.; Xiong, R.-G. Multichannel control of multiferroicity in single-component homochiral organic crystals. *J. Am. Chem. Soc.* **2021**, *143*, 21685−21693.

(36) Han, X.-B.; Chai, C.-Y.; Liang, B.-D.; Fan, C.-C.; Zhang, W. Ferroic phase transition molecular crystals. *CrystEngComm* **2022**, *24*, 1507−1517.

(37) Ranjan, S.; Takamizawa, S. Two-Dimensional Organoferroelasticity in a Single Crystal of 4-Iodoaniline. *Cryst. Growth Des.* **2022**, *22*, 1831−1836.

(38) Wang, Y.; Ren, J. Strain-driven switchable thermal conductivity in ferroelastic $PdSe_2$. *ACS Appl. Mater. Interfaces* **2021**, *13*, 34724−34731.

(39) Ding, X.; Salje, E. Heat transport by phonons and the generation of heat by fast phonon processes in ferroelastic materials. *AIP Adv.* **2015**, *5*, 053604.

(40) Hasija, A.; Ranjan, S.; Guerin, S.; Mangalampalli, S. K.; Takamizawa, S.; Chopra, D. Tracing shape memory effect and elastic bending in a conformationally flexible organic salt. *J. Mater. Chem. C* **2022**, *10*, 4257−4267.

(41) Ranjan, S.; Takamizawa, S. Characterization of Organo-ferroelasticity in a TEMPO Crystal. *Cryst. Growth Des.* **2022**, *22*, 585−589.

(42) (a) Ganis, P.; Martuscelli, E. The crystal and molecular structure of *trans*-2-butene-1, 4-dicarboxylic acid. *Ric. Sci.* **1966**, *36*, 439. (b) Hachuła, B.; Jabłońska, M.; Nowak, M.; Kusz, J. Redetermination of trans-*β*-hydromuconic acid. *Acta Crystallogr. C Struct. Chem.* **2008**, *64*, o459−o462.

(43) Honda, R.; Ryu, M.; Balčytis, A.; Vongsvivut, J.; Tobin, M. J.; Juodkazis, S.; Morikawa, J. Paracetamol micro-structure analysis by optical mapping. *Appl. Surf. Sci.* **2019**, *473*, 127−132.

(44) Hikima, Y.; Morikawa, J.; Hashimoto, T. Imaging of two-dimensional distribution of molecular orientation in poly (ethylene oxide) spherulite using IR spectrum and birefringence. *Macromolecules* **2012**, *45*, 8356−8362.

(45) Hikima, Y.; Morikawa, J.; Hashimoto, T. FT-IR image processing algorithms for in-plane orientation function and azimuth angle of uniaxially drawn polyethylene composite film. *Macromolecules* **2011**, *44*, 3950−3957.

(46) Ryu, M.; Balčytis, A.; Wang, X.; Vongsvivut, J.; Hikima, Y.; Li, J.; Tobin, M. J.; Juodkazis, S.; Morikawa, J. Orientational mapping augmented sub-wavelength hyper-spectral imaging of silk. *Sci. Rep.* **2017**, *7*, 7419.

(47) Sasaki, R.; Takahashi, Y.; Hayashi, Y.; Kawauchi, S. Atomistic Mechanism of Anisotropic Heat Conduction in the Liquid Crystal 4-Heptyl-4′-cyanobiphenyl: All-Atom Molecular Dynamics. *J. Phys. Chem. B* **2020**, *124*, 881−889.

(48) Sheldrick, G. M. SHELXT-Integrated space-group and crystal-structure determination. *Acta Crystallogr. A: Found. Adv.* **2015**, *71*, 3−8.

(49) Sheldrick, G. M. Crystal structure refinement with SHELXL. *Acta Crystallogr. C Struct. Chem.* **2015**, *71*, 3−8.

(50) Ryu, M.; Takamizawa, S.; Morikawa, J. Thermal diffusivity of organosuperelastic soft crystals during stress-induced phase transition. *Appl. Phys. Lett.* **2021**, *119*, 251902.

EDGE ARTICLE

Check for updates

A role of intermolecular interaction modulating thermal diffusivity in organosuperelastic and organoferroelastic cocrystals†

Subham Ranjan, [ID] [a] Ryota Morioka,[b] Meguya Ryu,[c] Junko Morikawa [ID] *[b] and Satoshi Takamizawa [ID] *[a]

Although the finding of superelasticity and ferroelasticity in organic crystals has been serendipitous, an increasing number of organic crystals with such deformation properties have been witnessed. Understanding the structure–property relationship can aid in the rational selection of intermolecular interactions to design organic crystals with desired superelastic or ferroelastic properties. In this study, we investigated the mechanical deformation in two cocrystals, prepared with the parent compound, 1,4-diiodotetrafluorobenzene with two coformers, 1,2-bis(4-pyridyl)ethane and pyrene. The parent compound and coformers were chosen to introduce distinct weak interactions such as halogen bonds and C−H···F, and π···π interactions in the crystal structure. The two cocrystals exhibited different mechanical deformations, superelasticity, and ferroelasticity, respectively. The single-crystal X-ray diffraction and energy framework analysis of the crystal structure of the cocrystals revealed that both deformations were caused by mechanical twinning. Interestingly, a difference in the extent of deformation was observed, modulated by a combination of strong and weak intermolecular interactions in the superelastic cocrystal, and only weak interaction in the ferroelastic one. In this comparison, the superelastic cocrystal exhibited higher thermal diffusivity than the ferroelastic cocrystal, indicating the presence of symmetrical and relatively robust intermolecular interactions in the superelastic cocrystal.

Introduction

Over the last decade, distinct mechanical deformation behavior in organic molecular crystals has been reported, thereby making them a prospective candidate as next-generation structural materials for actuators,[1] multi-stimuli responsive sensors,[2] optical waveguides,[3] and soft robotics.[4] Organic molecular crystals have been found to exhibit several mechanical deformation behaviors such as elastic and plastic bending,[5–7] light-induced bending,[8,9] superelasticity[10–12]

[a]Department of Materials System Science, Graduate School of Nanobioscience, Yokohama City University, 22-2 Seto, Kanazawa-ku, Yokohama, Kanagawa 236-0027, Japan. E-mail: staka@yokohama-cu.ac.jp

[b]Department of Materials Science and Engineering, School of Materials and Chemical Technology, Tokyo Institute of Technology, Tokyo 152-8550, Japan. E-mail: morikawa.j.aa@m.titech.ac.jp

[c]National Metrology Institute of Japan (NMIJ), National Institute of Advanced Industrial Science and Technology (AIST), Tsukuba Central 3, 1-1-1 Umezono, Tsukuba 305-8563, Japan

† Electronic supplementary information (ESI) available: Detailed information about the experimental section, and thermal and crystallographic studies (pdf). Movie S1: shear stress-induced mechanical deformation on the (0$\bar{1}$1) plane of cocrystal **1** by using a pair of tweezers. Movie S2: shear stress-induced mechanical deformation on the (001) plane of cocrystal **2** by using a pair of tweezers. CCDC 2256404–2256407. For ESI and crystallographic data in CIF or other electronic format see DOI: https://doi.org/10.1039/d3sc03155a

ferroelasticity,[13,14] superplasticity,[15] shape memory effect,[16,17] and many more. Superelastic and ferroelastic organic molecular crystals stand out as excellent and superior candidates in materials science due to their reversibility and diffusionless transformation behavior. Although both superelastic and ferroelastic deformations exhibit diffusionless transformation, the reversibility manner of the shape restoration differs. In superelastic deformation, the shape recovery is simply attained by removal of the applied force,[10] whereas in ferroelastic deformation, the shape change due to spontaneous strain is regained by application of force in the opposite direction to that of the deformation direction.[13] Digging into the mechanism, superelastic deformation is enabled by martensitic transformation,[10] whereas ferroelastic deformation is manifested by twinning deformation.[18] Recently, twinning has been found to be the common cause for both superelastic and ferroelastic deformation in organic crystals.[11,19]

While many organic molecular crystals exhibiting superelastic and ferroelastic deformation have been reported in recent years, a rational approach for designing and obtaining the desired superelastic and ferroelastic deformation is lacking.[10–13,20] For crystal structure designing with novel properties, a detailed understanding of various strong and weak molecular interactions is essential to modify the strength and geometry of intermolecular interactions. A thorough analysis

showed that different crystal structures with polar space groups and weak intermolecular interactions such as weak hydrogen bonding, halogen bonding, and van der Waals interactions contribute to superelastic or ferroelastic deformation.[20–22] The influence of weak intermolecular interactions involving halogen groups such as an aromatic C–F group,[23–26] and halogen–halogen[27,28] and π stacking interactions[29–31] on directing the crystal packing in the presence or absence of strong hydrogen bonds has been extensively studied, and can serve as an excellent tool for crystal designing. Li et al. suggested that such crystals could be designed by considering the orientational change of molecules caused by twinning in superelastic and ferroelastic deformation.[32] They prepared a cocrystal composed of 3,5-dimethylbenzoic acid and 4,4′-bipyridine bonded by an acid-pyridine hetero-synthon and resembling an organic trimer, which demonstrated a bidirectional superelastic deformation through a 90° rotation of the aromatic plane of 4,4′-bipyridine.[32] In our previous report about the shape memory effect of 1,2-bis(4pyridyl)ethane dodecafluorosuberate,[17] we realized that the introduction of weak dispersive interactions like C–F···π, and C–H···F in the crystal structure changed the deformation behavior from biased ferroelastic[33] to the shape memory effect (interconversion of superelastic to ferroelastic). In this case, this weak dispersion interaction combined with strong hydrogen bonding N⁺–H···O⁻ contributed to the shape memory effect with an increased critical forward stress value. Thalladi et al. mentioned that C–H···F interactions could be exploited to construct desirable organic crystals as compared to well-known C–H···O and C–H···N interactions owing to their ability to stabilize the crystal structures.[34] Additionally, Jain et al. demonstrated the role of halogen bonds in synthesizing higher-order cocrystals and further established that halogen bonds can exhibit analogous behavior to hydrogen bonds.[35] Mukherjee and Desiraju previously indicated that the strength of halogen bonds can manifest in elastic or plastic bending in organic crystals.[36] Thus, halogen bond-mediated/directed synthesis of a supramolecular assembly could be a possible way to design organic molecular crystals with desired superelastic and ferroelastic deformation. Variations in the strength of halogen bonds with excellent directionality[37] and other weak dispersive interactions[38] can manipulate the spontaneous strain generation required for ferroelastic deformation and spontaneous shape recovery in a superelastic deformation.

In addition to developing the designing principles for superelastic and ferroelastic deformation, studying the anisotropic thermal transport properties of these materials such as thermal diffusivity would be insightful owing to the range of thermal management applications of these crystals.[39,40] Previous studies have reported that the anisotropic mechanical properties of soft materials in response to high frequency can be correlated with thermal diffusivity.[41,42] Studying the anisotropic thermal properties in ferroelastic and superelastic organic crystals would be beneficial to understand the manner of heat transport with respect to their structural order. Furthermore, the reversible phase transition properties of these crystals in response to mechanical stress can be utilized as thermal switches.[43,44] The micro-level miniaturization of the integrated

devices demands efficient flexibility and thermal management, which can be fulfilled by the controlled deformation behavior of these crystals and used as wearable devices.[45–47] It has been demonstrated that inorganic ferroelastic materials can be utilized for thermal management applications.[44,48–50] Sieradzki et al. studied the changes in the thermal conductivity of Li_2-$TiGeO_5$ ceramics in the ferroelastic phase transition or domain formation.[50] Wang et al. reported the difference in thermal conductivity values of layered $PdSe_2$ before and after ferroelastic phase transition by uniaxial compression and demonstrated that the high ratio of the switchable thermal conductivity value between the two phases could be utilized for flexibility and thermal management.[44] However, there is only one study concerning the measurement of anisotropic heat transport properties in a superelastic organic crystal due to the limited approaches/techniques to measure the thermal diffusivity of organic crystals.[40]

Keeping these considerations in mind, we attempted to prepare single crystals of two cocrystals consisting of a weak halogen bond donor and acceptor, where 1,4-diiodotetrafluorobenzene served as the halogen donor. It produced cocrystals with the halogen acceptor 1,2-bis(4-pyridyl)ethane (cocrystal **1**) and pyrene (cocrystal **2**), respectively. Different deformation behaviors, i.e., superelastic and ferroelastic deformation, were observed in **1** and **2**, respectively. The anisotropic thermal diffusivity values of the two cocrystals were measured by typical microscale temperature-wave analysis (μ-TWA). A difference in the combination of relatively strong halogen interactions (C–I···N) and weak interactions (C–H···F and π···π) in the crystal structure of the two cocrystals could be responsible for the different mechanical deformations and thermal diffusivity behaviors.

Results and discussion

Single crystal synthesis and characterization

For cocrystal preparation, a halogen bond donor, 1,4-diiodotetrafluorobenzene was selected as the parent compound. In previous studies, 1,4-diiodotetrafluorobenzene has been utilized to prepare supramolecular structures owing to its ability to form a range of interactions, including C–I···N, C–H···F, and π···π.[51] Such weak C–H···F, C–F···π interactions can form crystal packing even in the absence of strong hydrogen bonds.[52] Furthermore, the C–I···N interactions have been demonstrated to be strong and directional to facilitate the self-assembly of a 1D infinite network, and other interactions such as C–H···F and π···π enable the formation of a 3D network.[53] In addition, Corradi et al. noted that the halogen bonding of 1,4-diiodotetrafluorobenzene was significantly accountable for the supramolecular structure formation with 1,2-bis(4-pyridyl)ethane and hydroquinone compared to hydrogen bonding.[51] In order to manipulate the weak interactions in the crystal structure, two coformers of 1,2-bis(4-pyridyl)ethane and pyrene were selected on the basis of halogen bond acceptor strength. 1,2-Bis(4-pyridyl)ethane acts as a strong halogen acceptor due to the electron rich nitrogen atom, while pyrene acts as a weak

halogen acceptor due to the absence of an electron rich group in its structure.

The colorless block shape single crystals of cocrystal **1** were obtained by slow evaporation of a dichloromethane solution of 1,4-diiodotetrafluorobenzene and 1,2-bis(4-pyridyl)ethane mixed at a molar ratio of 1 : 1.[54] The single crystal of cocrystal **1** crystallizes in a triclinic crystal system with space group $P\bar{1}$. The molecules formed an infinite 1D chain *via* the C–I···N (4.898(4) Å, 175.6°) halogen bonds with $d(\text{I1}\cdots\text{N1}) = 2.795(3)$ Å in an ABAB manner along the *a* axis. Furthermore, weak C–H···F hydrogen bonds connect the nearby 1D chains to create a three-dimensional crystal structure along the *bc* plane (Fig. 1 and Table S1, ESI†).

On the other hand, the colorless block-shaped single crystals of cocrystal **2** were obtained by slow evaporation of an ethanolic solution of 1,4-diiodotetrafluorobenzene and pyrene mixed in a molar ratio of 1 : 1.[55] The single crystals of **2** crystallize in

a monoclinic crystal system with space group $P2_1/c$. The single crystal of cocrystal **2** formed a column-like structure *via* π–π stacking in an A···B···A···B··· face-to-face manner along the *a* axis with an interplanar distance of 3.450 Å. Furthermore, the adjacent columns are linked together by C–I···I–C (3.812(6) Å) interactions along the *b* axis (Fig. 1 and Table S1, ESI†). The shortest C–H···F interactions (2.56 Å, 145.05°) were found along the *c* axis, stabilizing the crystal structure of **2**. The structures of cocrystals **1** and **2** along with their deformation behaviors are illustrated in Fig. 1.

Microscopic observation

For studying the shear deformation behavior at a macroscopic level, mechanical shear stress on both the single crystals of **1** and **2** was applied independently at room temperature under a polarized microscope on the (0$\bar{1}$1) plane and (001) plane,
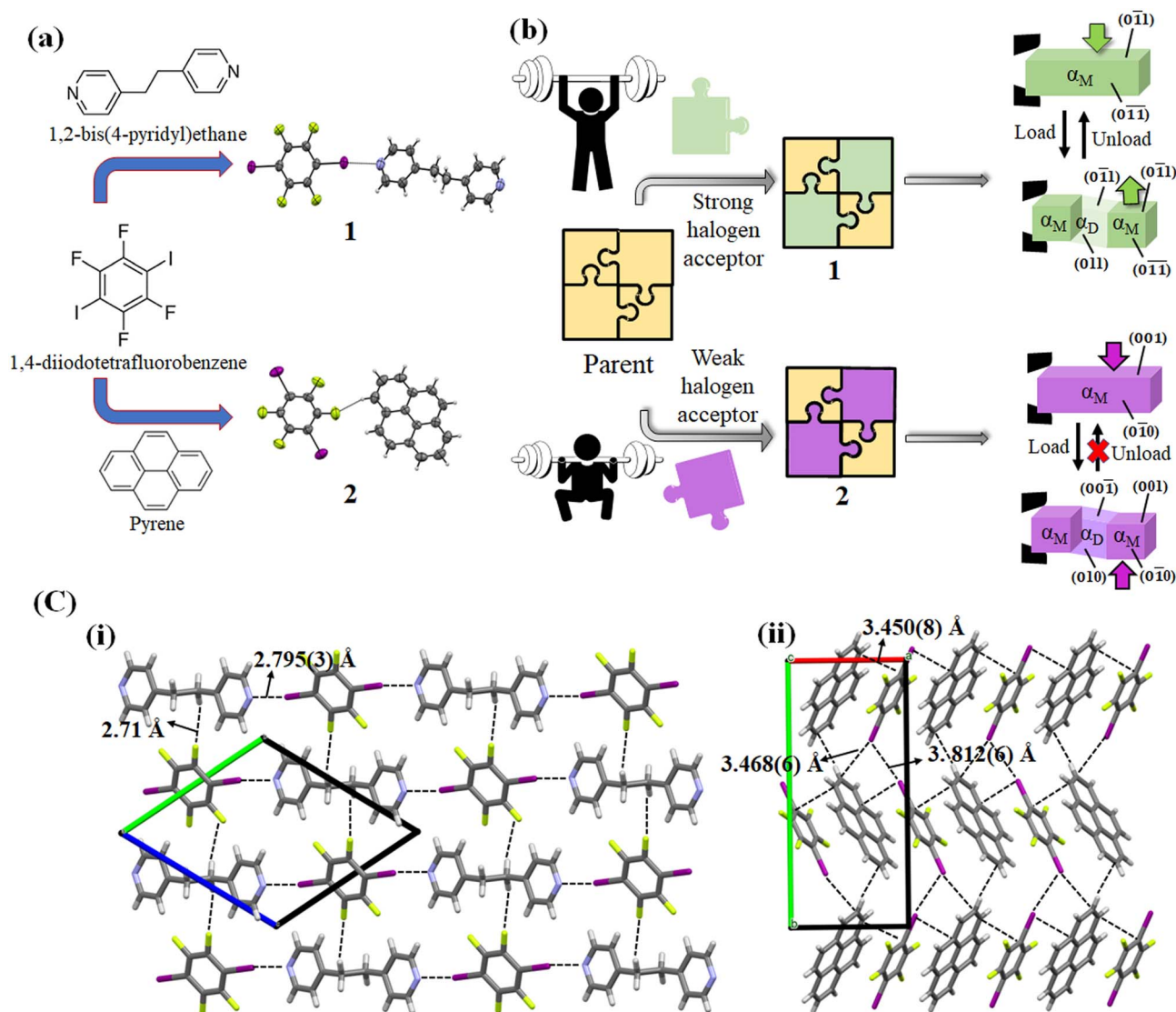

Fig. 1 (a) Molecular structures and formation of cocrystals **1** and **2**, (b) illustration of the difference in the mechanical deformation of interest, and (c) crystal structures of (i) cocrystal **1** along the *bc* plane and (ii) cocrystal **2** along the *a* axis.
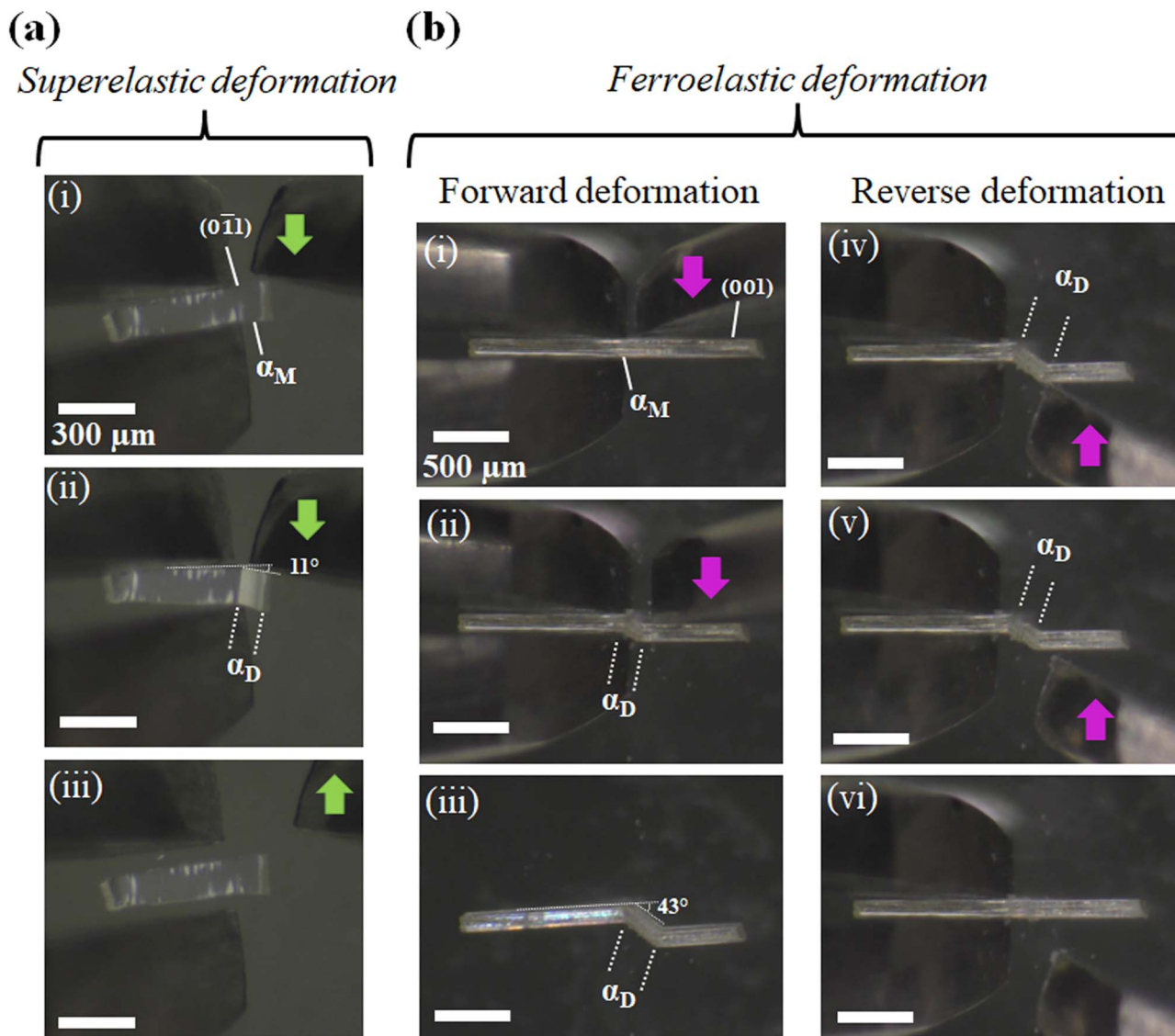
Fig. 2 Microscope observation with tweezers at room temperature: (a) superelastic deformation of cocrystal **1** and (b) ferroelastic deformation of cocrystal **2**.

respectively (Fig. 1(b)). An application of shear stress on the $(0\bar{1}1)$ plane of single crystals of **1** caused a superelastic deformation (Fig. 2(a)). The superelastic deformation was initiated by the appearance of a stress-induced twinning domain (α_D) generated from the mother crystal (α_M) with a distinct boundary line at a bending angle of 11°. The deformed crystal was recovered to its original shape after the applied force was removed. On the other hand, single crystals of **2** showed a ferroelastic deformation on the application of shear stress on the (001) plane (Fig. 2(b)). A bending angle of 43° was demonstrated with the growth of daughter domains (α_D) from the mother domain (α_M) in the single crystal of **2**, and a spontaneous strain was accumulated as residual strain until the removal of the force. Furthermore, on application of reverse force on the $(00\bar{1})$ plane, the daughter domain returned to its initial orientation, confirming the ferroelasticity.

Mechanical deformation analysis

The stress–strain relationship between cocrystals **1** and **2** was investigated by using a custom-designed setup: the shear force was applied with a jig to the specific crystal plane of the crystal fixed to a glass plate with epoxy glue. In a single crystal specimen of **1**, the α_D domain started to grow from the α_M domain at an applied stress of 0.27 MPa on the $(0\bar{1}1)$ plane. At a critical stress of 0.27 MPa, the stress-induced twinning phase transformation (α_D) propagated, and the stress–strain curves displayed a characteristic plateau resembling a superelastic deformation (Fig. 3(a)). The original shape was regained by decreasing the stress in depicting the typical superelastic stress–strain hysteresis loop, validating the superelastic deformation. On the other hand, with the gradual increase of stress on the (001) plane of the single crystal of **2**, the α_D domain was generated at a coercive stress of 0.58 MPa, which was fairly
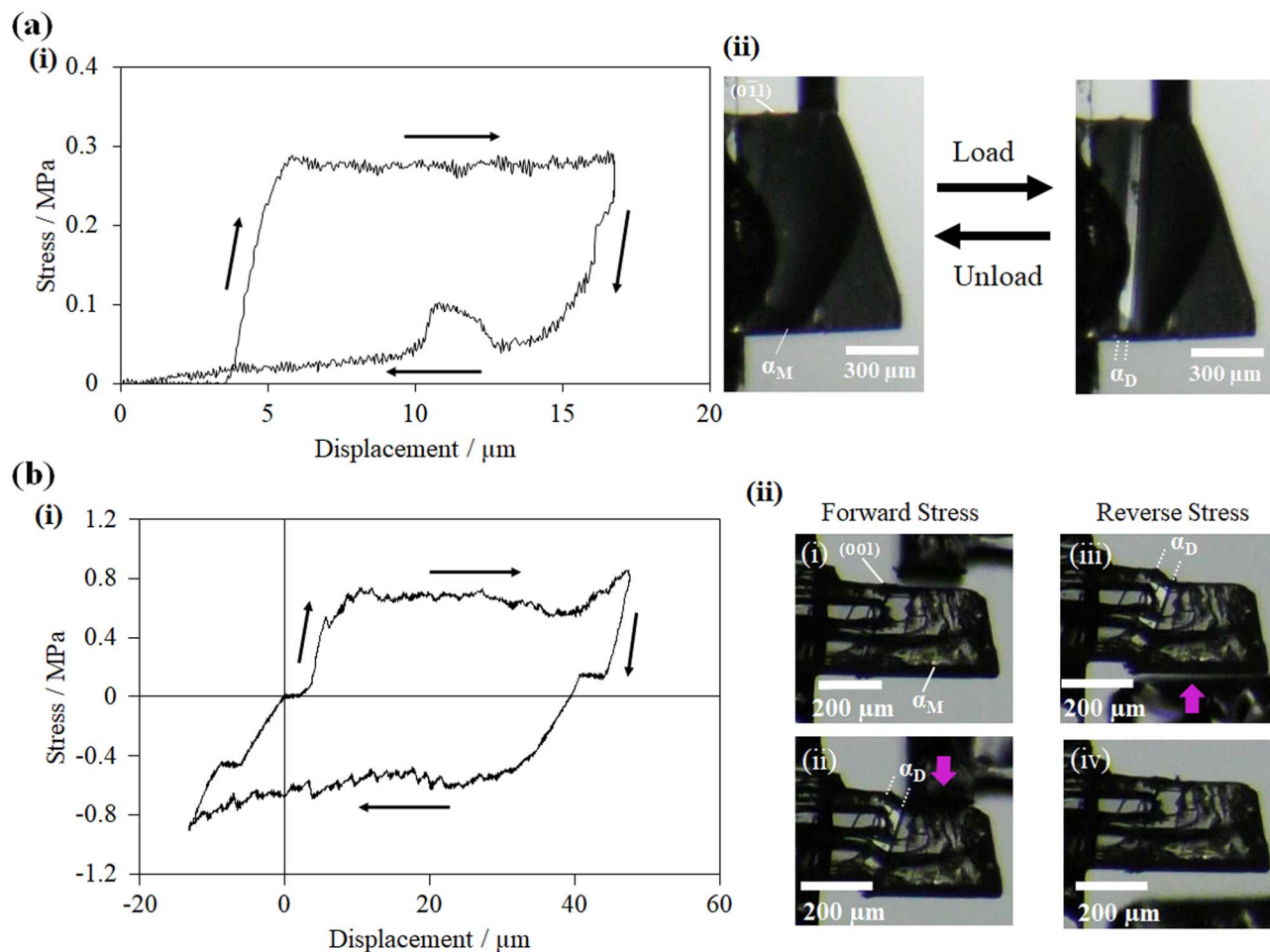
Fig. 3 Shear–strain test: (a) the superelastic hysteresis loop of the cocrystal of **1** (i) and snapshots during measurement (ii) and (b) the ferroelastic hysteresis loop of the cocrystal of **2** (i) and snapshots (ii).

steady. Furthermore, by applying a shear stress of 0.57 MPa force from the opposite direction, the α_D domain was reverted to the α_M domain with the corresponding release of the spontaneous strain. The hysteresis loop was established in the shear displacement graph, which is the confirmatory indicator of ferroelastic deformation (Fig. 3(b)). The observed stress strengths are similar to those of organosuperelastic/ organoferroelastic crystals previously reported.[13–19]

Thermal diffusivity studies

Thermal diffusivity is a specific property of materials related to the rate of thermal energy transfer through it. Determination of the thermal diffusivity value of the crystals would aid in understanding the heat transfer properties and their applicability in thermal management. In addition, it can also assist in understanding the changes in the thermal properties due to the structure, phase transitions, defects, *etc.* The anisotropic thermal diffusivity measurement of single crystals **1** and **2** were performed by μ-TWA measurements[40] along its longer, wider, and thinner axis. The frequency change in the phase delay of the temperature wave was obtained for the three crystallographic axes of the crystals (Fig. 4, S1, S2, and Tables S2, S3, ESI†).

From the measured data, the slope of the high-frequency region, which was decided according to the linearity of both phase and amplitude data, was used to determine the thermal diffusivity. In single crystals of **1**, the measured thermal diffusivity was found to be the highest 6.30×10^{-7} m² s⁻¹ along the $[0\bar{1}\bar{1}]$ direction followed by, 2.04×10^{-7} m² s⁻¹ along the $[0\bar{1}1]$ direction, and 1.12×10^{-7} m² s⁻¹ along the [100] direction (Fig. 5, S1, and Table S2, ESI†). In contrast, the thermal diffusivity of the ferroelastic crystal was similar along the $[0\bar{1}0]$ direction and [100] directions (0.93×10^{-7} m² s⁻¹). However, a lower thermal diffusivity was observed along the [001] direction (0.69×10^{-7} m² s⁻¹) which is the shear stress deformation direction of cocrystal **2** (Fig. 5, S2, and Table S3, ESI†). The highest obtained thermal diffusivity along the $[0\bar{1}0]$ direction in the ferroelastic crystal was almost 7-fold lower compared to that of superelastic crystal along the $[0\bar{1}\bar{1}]$ direction. In addition, the thermal diffusivity value of both the crystals was low in the direction of applied shear stress along $[0\bar{1}1]$ of **1** and [001] of **2** compared to their orthogonal directions. Furthermore, the thermal diffusivity values in the daughter domains of cocrystals **1** and **2** were found to increase by 17% (7.38×10^{-7} m² s⁻¹) and 7% (0.99×10^{-7} m² s⁻¹) along the $[0\bar{1}0]$ and $[0\bar{1}\bar{1}]$ directions of **1**
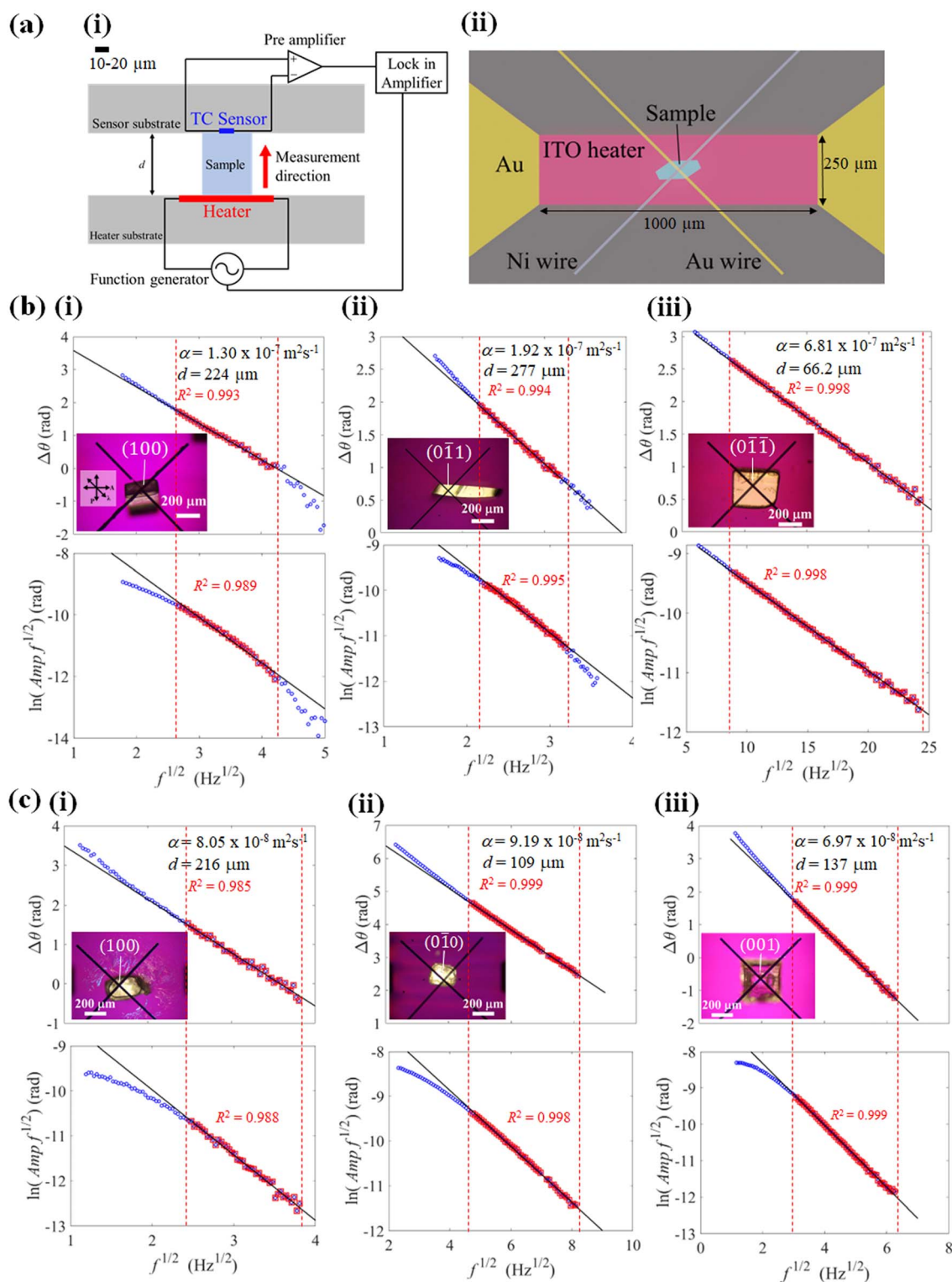
Fig. 4 The frequency dependency of the phase delay measured for cocrystals **1** and **2** (a) schematic depiction of the experimental setup from the (i) cross-sectional view and (ii) top-view. The synchronized function generator and the lock-in amplifier determined the periodic heating and detection of the periodic temperature response from the sample as a phase delay. (b) (i), (ii), and (iii) cocrystals of **1** placed along its longer, wider and thinner axes corresponding to the [100], [0$\bar{1}$1] and [0$\bar{1}\bar{1}$] directions, respectively, and (c) (i), (ii), and (iii) cocrystals of **2** placed along its longer, wider and thinner axes corresponding to the [100], [0$\bar{1}$0], and [001] directions, respectively. The inset shows the optical image of each sample under a crossed-Nicols with a sensitive plate (530 nm wave plate) taken by using a polarized microscope (top view).
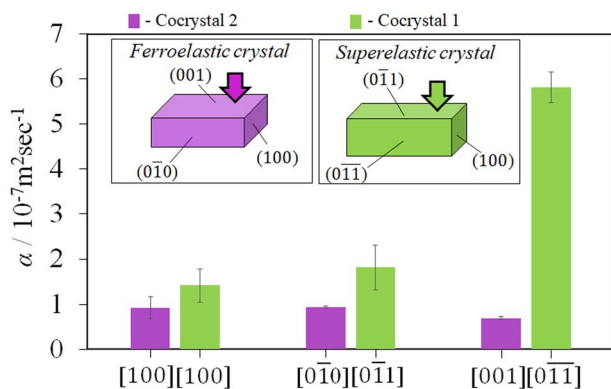
Fig. 5 The obtained thermal diffusivity values of cocrystals **1** (light green colored) and **2** (purple colored) with respect to the longer, wider, and thinner axes, respectively. Arrows indicate the direction of shear stress deformations.

and **2**, respectively (Fig. S3, Table S4, ESI†). The switchable thermal diffusivity values of the mother and daughter domains indicate the potential for a thermal switch application of these crystals.

Crystallographic studies

The underlying mechanism behind the different deformation behaviors of cocrystals **1** and **2** were investigated by single-crystal XRD analyses of the deformed crystals of **1** and **2**. The cocrystal of **1** crystallizes in a triclinic crystal system with the space group $P\bar{1}$. On the other hand, the cocrystal of **2** crystallizes in a monoclinic crystal system with space group $P2_1/c$. Both the crystal structures were similar to the previously reported one.[51,55] XRD investigations of **1** and **2** using face indexing revealed that the shear-induced twinning deformation initiated the development of the daughter crystal domain (α_D) from the mother crystal domain (α_M) upon application of shear stress on the ($0\bar{1}1$) and (001) planes, respectively (Fig. 6, 7, S4 and Table S1, ESI†). According to crystallographic investigations, the twinning interfaces of cocrystals **1** and **2** are located at $(100)\alpha_M/(100)\alpha_D$ and $(10\bar{1})\alpha_M/(\bar{1}01)\alpha_D$, respectively, which are perpendicular to the stacked column. A 180° rotation about the rotation axis was associated with the mother domain and daughter domains. This relationship is attributed to the polar $P\bar{1}$ and $P2_1/c$ point group symmetry, which caused the molecules to tilt by 41.81° of the 1,4-diiodotetrafluorobenzene molecule and 7.81° of 1,2-bis(4-pyridyl)ethane molecule in the case of cocrystal **1**, and 57.48° of the 1,4-diiodotetrafluorobenzene molecule and 63.48° of the pyrene molecule in the case of cocrystal **2**, instead of the actual 180° rotation (Fig. S4, ESI†). 1,4-diiodotetrafluorobenzene interacted through C–I⋯N and C–H⋯F interactions with the nearby molecules in crystal structure **1**, where it is surrounded by four 1,2-bis(4-pyridyl)ethane molecules in a rhomboid configuration with sides of 10.401 Å and 7.379 Å (Fig. 6(b)(ii)). 1,4-diiodotetrafluorobenzene was rotated by 41.81° in relation to its mother domain configuration due to the twinning orientational change. As a result, the crystal structure is balanced and has a configuration analogous to a rhomboid
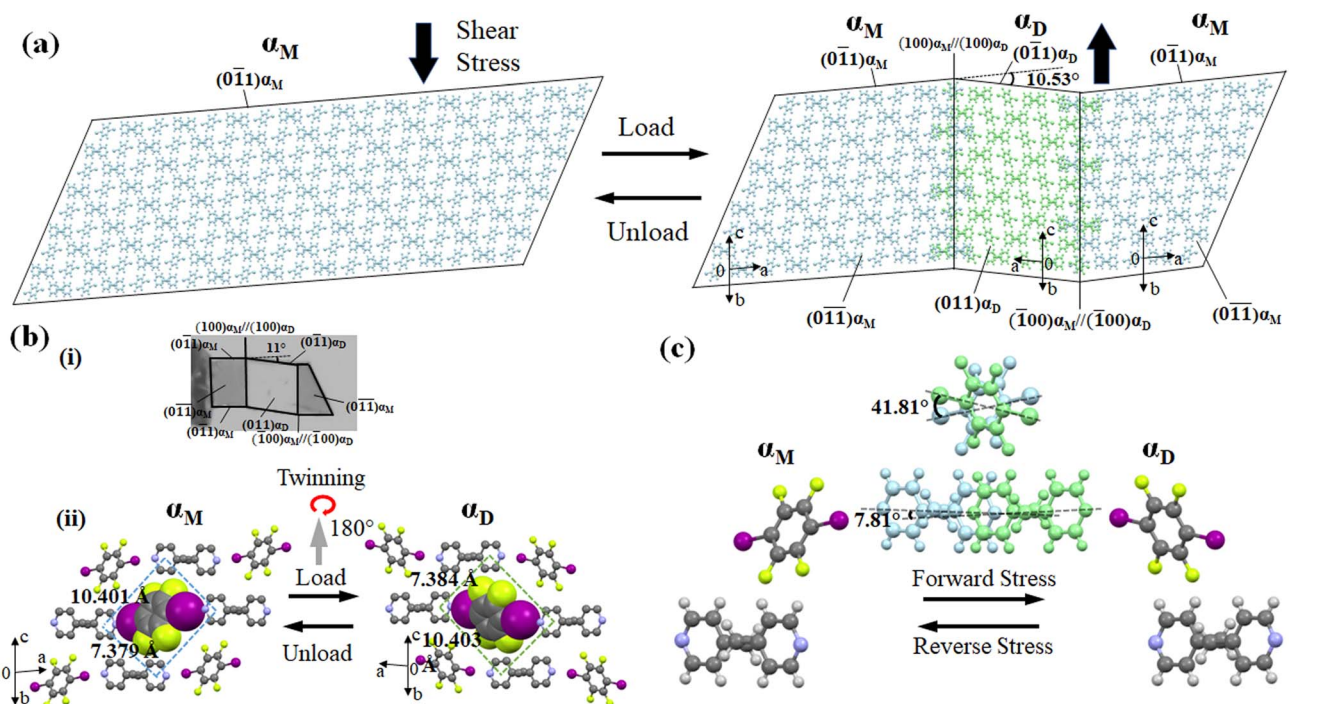

Fig. 6 (a) Estimated connecting manners of the α_M domain and α_D domain based on the X-ray diffraction measurements of single crystal **1**. (b) Face indexing of the superelastic bent crystal used for SCXRD (i) and estimated twinning manners of the α_D domain based on the α_M domain (ii). (c) Estimated molecular movements at the interface at $(100)\alpha_M//(100)\alpha_D$ (light blue and light green colored molecules indicate the α_M and α_D domains, respectively).
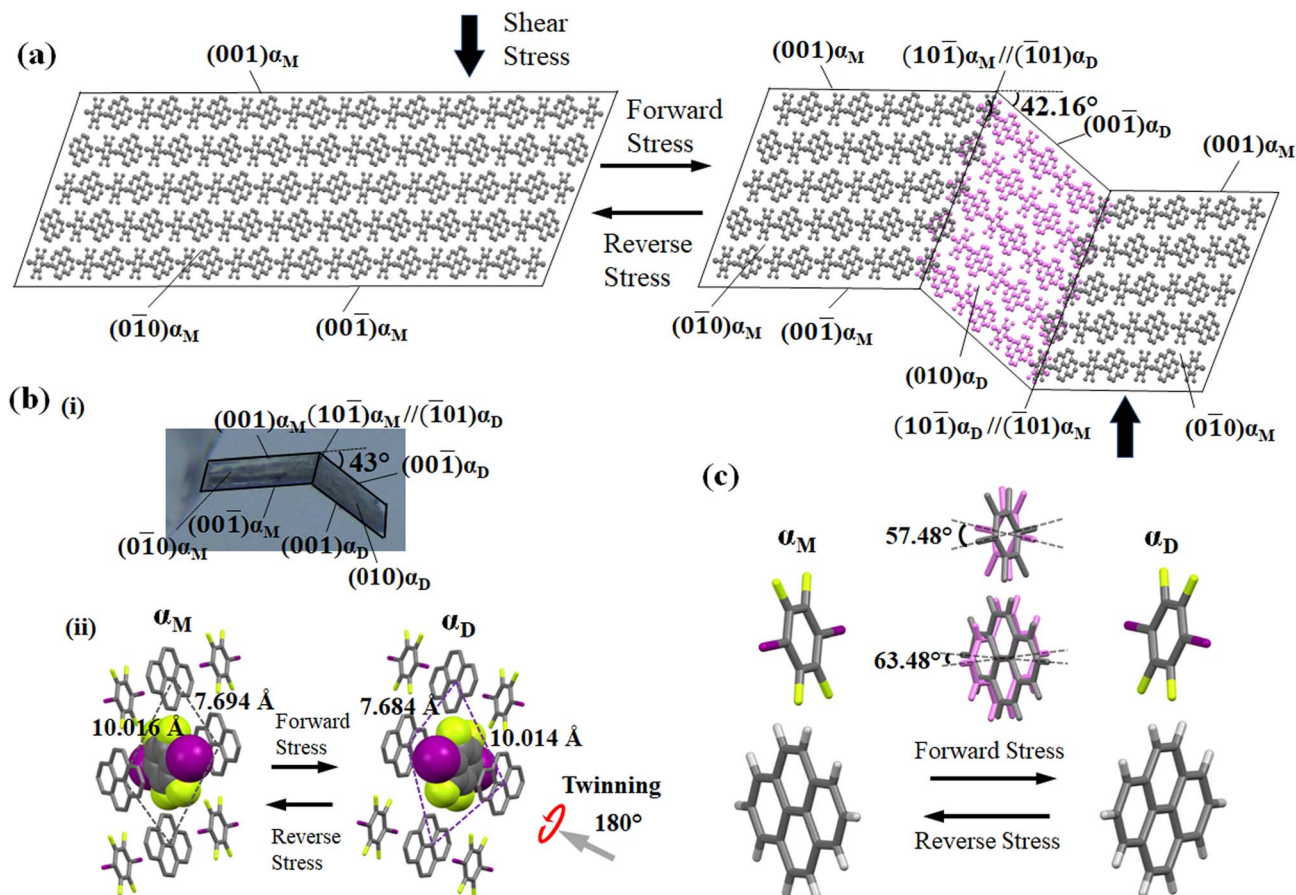
Fig. 7 (a) Estimated connecting manners of the α_M domain and α_D domain based on the X-ray diffraction measurements of single crystal **2**. (b) (i) Face indexing of the ferroelastic bent crystal used for SCXRD. (ii) Estimated twinning manners of the α_D domain based on the α_M domain. (c) Estimated molecular movements at the interface at (10$\bar{1}$) α_M/($\bar{1}$01)α_D. Light gray and light purple colored molecules indicate the α_M and α_D domains, respectively.

arrangement rotated by 90° in the daughter phase with sides of 7.384 Å and 10.403 Å. Similar observations were seen for cocrystal **2**, which also resembled a tunable rhomboid structure with sides of 10.016 Å and 7.694 Å in the mother domain and 7.684 Å and 10.014 Å in the daughter domain (Fig. 7(b)(ii)).

Although mechanical twinning manifested superelastic and ferroelastic deformations in both crystals, the deformation produced a different bending angle and dissipated energy (E_d). A bending angle of 10.53° between α_M and α_D can be anticipated based on crystallographic results in cocrystal **1**, and this angle aligned well with the 11° bending angle that was measured by optical microscopy. However, the bending angle was higher by 32° in the case of cocrystal **2** compared to cocrystal **1**, which was estimated to be 42.16° by crystallographic analysis and 43° by optical microscopy. Due to the molecular movement by such a large angle, significant coercive stress was observed during the daughter domain development in ferroelastic deformation. Furthermore, the lower tilt angle of molecules in the case of molecule **1** could be due to the presence of relatively strong and ordered C–I⋯N (4.898(4) Å, 175.6°) halogen interactions, and the stable twisted chair form of bipyridine moieties which would stabilize the crystal during the application of stress.

In cocrystal **1**, the strong C–I⋯N halogen bond is clarified by the shorter I–N (2.795(3) Å) distance compared to other bipyridine-based halogen bonded complexes, relating to the two distantly placed twisted chair forms of the bipyridine rings in the structure. The strong C–I⋯N halogen-bonded interactions and weak C–H⋯F (3.528(3) Å, 141.98° (F1⋯H6a (2.71 Å))) hydrogen-bonded interactions in cocrystal **1** can make its crystal packing robust compared to cocrystal **2** (Fig. 8(a)).

In cocrystal **2**, C–I/I–C (d(I–I) 3.812(6) Å) interactions hold the parallel-placed columns together. The connectivity between columns appears to be strengthened by C–I⋯π (3.468(6) Å) halogen bonding and C–H⋯F (3.367(5) Å, 145.05°) interactions d(F1⋯H19) = 2.56 Å to maintain the 3D crystal structure (Fig. 8(b)).

Correlation of anisotropic structural arrangement with mechanical behavior and thermal diffusivity

Since cocrystals **1** and **2** have a diversity of contacts, including halogen, π⋯π, and C–H⋯F interactions, it can be anticipated that the forces retaining them are diverse in strength. Hirshfeld surface analysis was utilized to evaluate the relative efficacy of the competing weak hydrogen bonding, π⋯π, and halogen-
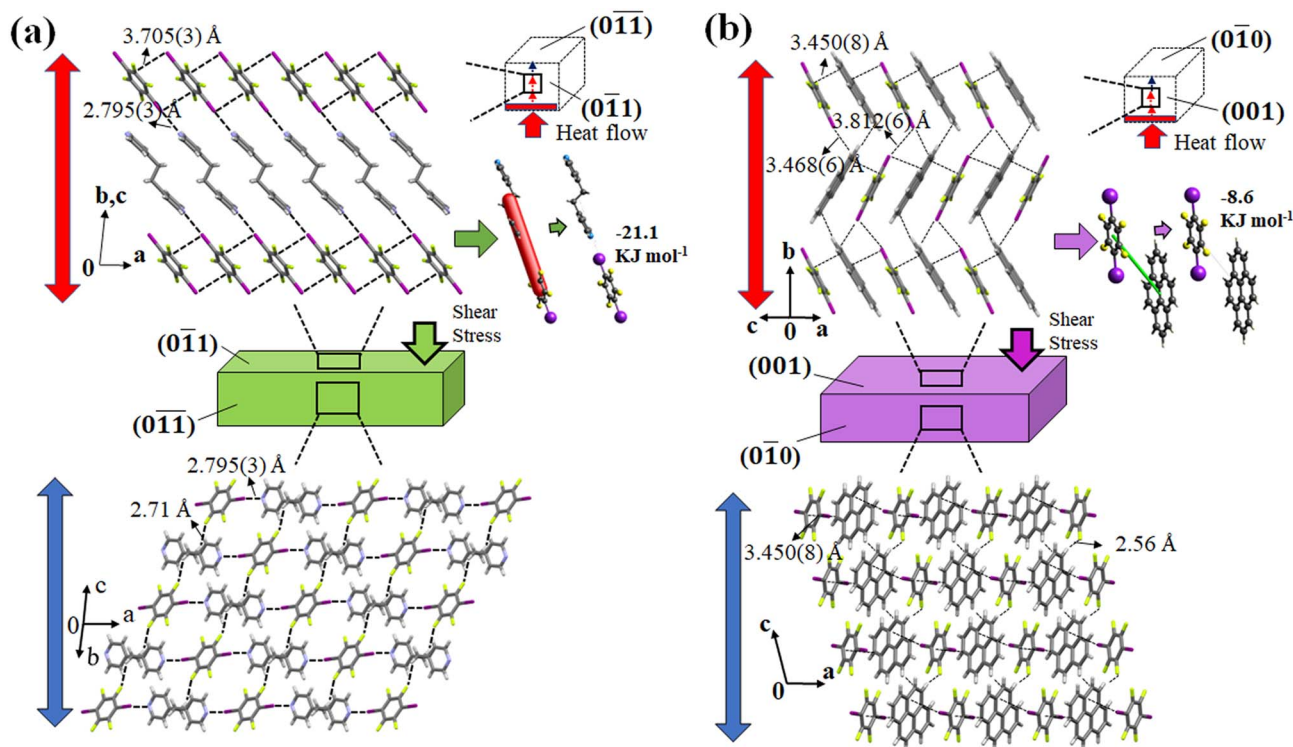
Fig. 8 Crystal packing with the 3D topology of energy frameworks of cocrystal 1 (i) and 2 (ii). Red and blue colored bidirectional arrows indicate the highest and lowest thermal diffusivity direction of cocrystals 1 and 2, respectively. Red and green colored tubes indicate the electrostatic and dispersion energy, respectively.

bonding interactions (Fig. S5, ESI†). Short interactions were discovered to be distinct in the mother phase of cocrystals 1 and 2. In cocrystal 1, the F···H (34.6%) interaction was found to be the highest interaction supporting the three-dimensional structure, followed by I···H (9.8%), C···I (9.1%), and I···N (4.7%) interactions. Nevertheless, the contributions of all interactions changed in cocrystal 2. However, F···H (23.4%) interaction was also seen to be the highest in cocrystal 2 followed by I···H (15.3%) and C···C (11.8%) interactions. It can be inferred that the halogen and weak hydrogen bond interactions play a significant role in determining the crystal structure of 1. On the other hand, weak hydrogen bonds and π···π interactions play a crucial role in maintaining the crystal structure of 2. Furthermore, energy framework analysis suggests that the C–I···N halogen interaction in cocrystal 1 is a strong, electrostatically dominant interaction with an energy of -21.1 kJ m^{-1} that holds the structure together with weak C–H···F interactions (Fig. 8(a) and S6, ESI†). In contrast, weak electrostatic C–I/C–I interactions were found to be accompanied by the presence of the dispersion-dominated C–H···F and π···π interactions in cocrystal 2, which have a -8.6 kJ mol^{-1} energy along the ac plane (Fig. 8 and S7, ESI†). The comparatively stronger interactions such as C–I···N, C–I, and C–H···F in cocrystal 1 could have promoted the superelastic deformation rather than ferroelastic deformation. Furthermore, the C–I···N halogen interaction tapes that make 2D sheets with the help of C–H···F interactions grow along the $[0\bar{1}\bar{1}]$ direction in a symmetrical stack in cocrystal 1. This could be the reason for the highest

thermal diffusivity along the $[0\bar{1}\bar{1}]$ direction where the robust, strong, and electrostatically dominated C–I···N halogen bonds determine the thermal diffusivity value. In contrast, dispersion dominated C–I/C–I and π···π interactions contained in cocrystal 2 resulted in its lower thermal diffusivity than that of cocrystal 1.

Conclusions

In conclusion, we presented two cocrystals consisting of (1,2-bis(4-pyridyl)ethane and 1,4-diiodotetrafluorobenzene), and (pyrene and 1,4-diiodotetrafluorobenzene), which are denoted as 1 and 2, respectively. Cocrystals 1 and 2 demonstrated superelastic and ferroelastic deformations, respectively. From the crystal structure analysis, the underlying cause of the deformation was found to be mechanical twinning. The difference in the deformation behavior was discussed through the distinct combination of strong halogen bonds, such as C–I···N and C···I, and weak interactions, such as C–H···F and π···π interactions in the cocrystal structures. The thermal diffusivity measurements on the ferroelastic and superelastic crystals showed the axial-dependent anisotropic thermal diffusivity of the cocrystals. A 7-fold difference in thermal diffusivity was observed in superelastic crystal 1, the highest in the orthogonal plane to the shear-induced direction, whereas in crystal 2 the axial dependence was less pronounced. This study provides insights into the interplay with the variation of inter-molecular interactions in organosuperelastic and organoferroelastic

behavior and the way for further design and regulation of functional organic solids with thermo-mechanical properties.

Data availability

All experimental, thermal diffusivity, and crystallographic data are available in the ESI.†

Author contributions

S. R. carried out the experiments, analyzed the results, and composed the manuscript. R. M., M. R., and J. M. conducted thermal diffusivity investigations. J. M. and S. T. organized the project and edited the manuscript.

Conflicts of interest

The authors declare no competing financial interest.

Acknowledgements

References

1 L. Li, P. Commins, M. B. Al-Handawi, D. P. Karothu, J. M. Halabi, S. Schramm, J. Weston, R. Rezgui and P. Naumov, Martensitic organic crystals as soft actuators, *Chem. Sci.*, 2019, **10**, 7327–7332.

2 M. Xie, K. Hisano, M. Zhu, T. Toyoshi, M. Pan, S. Okada, O. Tsutsumi, S. Kawamura and C. Bowen, Flexible multifunctional sensors for wearable and robotic applications, *Adv. Mater. Technol.*, 2019, **4**, 1800626.

3 B. Tang, X. Yu, K. Ye and H. Zhang, Manifold mechanical deformations of organic crystals with optical waveguiding and polarization rotation functions, *Adv. Opt. Mater.*, 2022, **10**, 2101335.

4 H. Koshima, T. Taniguchi and T. Asahi, Mechanically responsive crystals by light and heat, in *Mechanically Responsive Materials for Soft Robotics*, 2020, pp. 57–82.

5 S. Ghosh and C. M. Reddy, Elastic and bendable caffeine cocrystals: implications for the design of flexible organic materials, *Angew. Chem., Int. Ed.*, 2012, **51**, 10319–10323.

6 R. Samanta, S. Das, S. Mondal, T. Alkhidir, S. Mohamed, S. P. Senanayak and C. M. Reddy, Elastic organic semiconducting single crystals for durable all-flexible field-effect transistors: insights into the bending mechanism, *Chem. Sci.*, 2023, **14**, 1363–1371.

7 G. R. Krishna, R. Devarapalli, G. Lal and C. M. Reddy, Mechanically flexible organic crystals achieved by introducing weak interactions in structure: supramolecular shape synthons, *J. Am. Chem. Soc.*, 2016, **138**, 13561–13567.

8 R. O. Al-Kaysi and C. J. Bardeen, Reversible photoinduced shape changes of crystalline organic nanorods, *Adv. Mater.*, 2007, **19**, 1276–1280.

9 J. K. Sun, W. Li, C. Chen, C. X. Ren, D. M. Pan and J. Zhang, Photoinduced bending of a large single crystal of a 1,2-bis(4-pyridyl) ethylene-based pyridinium salt powered by a [2 + 2] cycloaddition, *Angew. Chem., Int. Ed.*, 2013, **125**, 6785–6789.

10 S. Takamizawa and Y. Miyamoto, Superelastic organic crystals, *Angew. Chem., Int. Ed.*, 2014, **126**, 7090–7093.

11 S. Takamizawa and Y. Takasaki, Superelastic Shape Recovery of Mechanically Twinned 3, 5-Difluorobenzoic Acid Crystals, *Angew. Chem., Int. Ed.*, 2015, **127**, 4897–4899.

12 H. Sun, S. K. Park, Y. Diao, E. P. Kvam and K. Zhao, Molecular mechanisms of superelasticity and ferroelasticity in organic semiconductor crystals, *Chem. Mater.*, 2021, **33**, 1883–1892.

13 S. H. Mir, Y. Takasaki, E. R. Engel and S. Takamizawa, Ferroelasticity in an organic crystal: a macroscopic and molecular level study, *Angew. Chem., Int. Ed.*, 2017, **56**, 15882–15885.

14 S. Ranjan and S. Takamizawa, Two-dimensional organoferroelasticity in a single crystal of 4-iodoaniline, *Cryst. Growth Des.*, 2022, **22**, 1831–1836.

15 S. Takamizawa, Y. Takasaki, T. Sasaki and N. Ozaki, Superplasticity in an organic crystal, *Nat. Commun.*, 2018, **9**, 3984.

16 S. Takamizawa and Y. Takasaki, Shape-memory effect in an organosuperelastic crystal, *Chem. Sci.*, 2016, **7**, 1527–1534.

17 S. Ranjan, H. Honda and S. Takamizawa, Thermo-mechanical reversibility in a shape memory organic salt, *J. Mater. Chem. C*, 2022, **10**, 12765–12775.

18 E. R. Engel and S. Takamizawa, Versatile ferroelastic deformability in an organic single crystal by twinning about a molecular zone axis, *Angew. Chem., Int. Ed.*, 2018, **57**, 11888–11892.

19 T. Sasaki, S. Sakamoto, Y. Takasaki and S. Takamizawa, A Multidirectional Superelastic Organic Crystal by Versatile Ferroelastical Manipulation, *Angew. Chem., Int. Ed.*, 2020, **132**, 4370–4373.

20 S. K. Park, H. Sun, H. Chung, B. B. Patel, F. Zhang, D. W. Davies, T. J. Woods, K. Zhao and Y. Diao, Super-and ferroelastic organic semiconductors for ultraflexible single-crystal electronics, *Angew. Chem., Int. Ed.*, 2020, **132**, 13104–13112.

21 S. Ranjan and S. Takamizawa, Characterization of Organoferroelasticity in a TEMPO Crystal, *Cryst. Growth Des.*, 2021, **22**, 585–589.

22 T. Seki, C. Feng, K. Kashiyama, S. Sakamoto, Y. Takasaki, T. Sasaki, S. Takamizawa and H. Ito, Photoluminescent ferroelastic molecular crystals, *Angew. Chem., Int. Ed.*, 2020, **59**, 8839–8843.

23 M. D. Prasanna and T. N. Guru Row, C–halogen···π interactions and their influence on molecular

conformation and crystal packing: A database study, *Cryst. Eng.*, 2000, **3**, 135–154.

24 M. D. Prasanna and T. N. Guru Row, Analysis of weak interactions involving fluorine: a comparative study of crystal packing of some benzodiazepinone drug intermediates and their non-fluorinated analogues, *CrystEngComm*, 2000, **2**, 134–140.

25 D. Chopra and T. N. Guru Row, Evaluation of the interchangeability of C–H and C–F groups: insights from crystal packing in a series of isomeric fluorinated benzanilides, *CrystEngComm*, 2008, **10**, 54–67.

26 V. R. Hathwar, D. Chopra, P. Panini and T. N. Guru Row, Revealing the polarizability of organic fluorine in the trifluoromethyl group: implications in supramolecular chemistry, *Cryst. Growth Des.*, 2014, **14**, 5366–5369.

27 A. Mukherjee, S. Tothadi and G. R. Desiraju, Halogen bonds in crystal engineering: like hydrogen bonds yet different, *Acc. Chem. Res.*, 2014, **47**, 2514–2524.

28 T. Caronna, R. Liantonio, T. A. Logothetis, P. Metrangolo, T. Pilati and G. Resnati, Halogen Bonding and $\pi\cdots\pi$ Stacking Control Reactivity in the Solid State, *J. Am. Chem. Soc.*, 2004, **126**, 4500–4501.

29 H. Adams, J. L. Jimenez Blanco, G. Chessari, C. A. Hunter, C. M. Low, J. M. Sanderson and J. G. Vinter, Quantitative determination of intermolecular interactions with fluorinated aromatic rings, *Chem.–Eur. J.*, 2001, **7**, 3494–3503.

30 H. Adams, S. L. Cockroft, C. Guardigli, C. A. Hunter, K. R. Lawson, J. Perkins, S. E. Spey, C. J. Urch and R. Ford, Experimental measurement of noncovalent interactions between halogens and aromatic rings, *ChemBioChem*, 2004, **5**, 657–665.

31 S. E. Wheeler, Local nature of substituent effects in stacking interactions, *J. Am. Chem. Soc.*, 2011, **133**, 10262–10274.

32 Y. X. Li, Z. K. Liu, J. Cao, J. Tao and Z. S. Yao, Stress-Induced Inversion of Linear Dichroism by 4,4′-Bipyridine Rotation in a Superelastic Organic Single Crystal, *Angew. Chem., Int. Ed.*, 2023, **62**, e202217977.

33 T. Sasaki, S. Sakamoto, K. Nishizawa and S. Takamizawa, Ferroelasticity with a Biased Hysteresis Loop in a Cocrystal of Pimelic Acid and 1,2-Di(4-pyridyl) ethane, *Cryst. Growth Des.*, 2020, **20**, 3913–3917.

34 V. R. Thalladi, H.-C. Weiss, D. Bläser, R. Boese, A. Nangia and G. R. Desiraju, C–H···F Interactions in the crystal structures of some fluorobenzenes, *J. Am. Chem. Soc.*, 1998, **120**, 8702–8710.

35 H. Jain, D. Sutradhar, S. Roy and G. R. Desiraju, Synthetic Approaches to Halogen Bonded Ternary Cocrystals, *Angew. Chem., Int. Ed.*, 2021, **133**, 12951–12956.

36 A. Mukherjee and G. R. Desiraju, Halogen bonds in some dihalogenated phenols: applications to crystal engineering, *IUCrJ*, 2014, **1**, 49–60.

37 S. Chakraborty and G. R. Desiraju, C–H···F hydrogen bonds in solid solutions of benzoic acid and 4-fluorobenzoic acid, *Cryst. Growth Des.*, 2018, **18**, 3607–3615.

38 S. Saha, M. K. Mishra, C. M. Reddy and G. R. Desiraju, From molecules to interactions to crystal engineering: mechanical properties of organic solids, *Acc. Chem. Res.*, 2018, **51**, 2957–2967.

39 S. Hasebe, Y. Hagiwara, J. Komiya, M. Ryu, H. Fujisawa, J. Morikawa, T. Katayama, D. Yamanaka, A. Furube and H. Sato, Photothermally driven high-speed crystal actuation and its simulation, *J. Am. Chem. Soc.*, 2021, **143**, 8866–8877.

40 M. Ryu, S. Takamizawa and J. Morikawa, Thermal diffusivity of organosuperelastic soft crystals during stress-induced phase transition, *Appl. Phys. Lett.*, 2021, 119.

41 M. Ryu, Y. Cang, Z. Wang, G. Fytas and J. Morikawa, Temperature-dependent thermoelastic anisotropy of the phenyl pyrimidine liquid crystal, *J. Phys. Chem. C*, 2019, **123**, 17148–17154.

42 Y. Cang, J. Liu, M. Ryu, B. Graczykowski, J. Morikawa, S. Yang and G. Fytas, On the origin of elasticity and heat conduction anisotropy of liquid crystal elastomers at gigahertz frequencies, *Nat. Commun.*, 2022, **13**, 5248.

43 R. G. Xiong, S. Q. Lu, Z. X. Zhang, H. Cheng, P. F. Li and W. Q. Liao, A chiral thermochromic ferroelastic with seven physical channel switches, *Angew. Chem., Int. Ed.*, 2020, **59**, 9574–9578.

44 Y. Wang and J. Ren, Strain-driven switchable thermal conductivity in ferroelastic $PdSe_2$, *ACS Appl. Mater. Interfaces*, 2021, **13**, 34724–34731.

45 D. Zhang, Y. Mao, P. Bai, Q. Li, W. He, H. Cui, F. Ye, C. Li, R. Ma and Y. Chen, Multifunctional superelastic graphene-based thermoelectric sponges for wearable and thermal management devices, *Nano Lett.*, 2022, **22**, 3417–3424.

46 N. Li, J. Ren, L. Wang, G. Zhang, P. Hänggi and B. Li, Colloquium: Phononics: Manipulating heat flow with electronic analogs and beyond, *Rev. Mod. Phys.*, 2012, **84**, 1045.

47 Y. Li, W. Li, T. Han, X. Zheng, J. Li, B. Li, S. Fan and C.-W. Qiu, Transforming heat transfer with thermal metamaterials and devices, *Nat. Rev. Mater.*, 2021, **6**, 488–507.

48 S. Li, X. Ding, J. Ren, X. Moya, J. Li, J. Sun and E. K. Salje, Strain-controlled thermal conductivity in ferroic twinned films, *Sci. Rep.*, 2014, **4**, 6375.

49 X. Ding and E. Salje, Heat transport by phonons and the generation of heat by fast phonon processes in ferroelastic materials, *AIP Adv.*, 2015, **5**, 053604.

50 A. Sieradzki, A. Jeżowski and R. Poprawski, The influence of ferroelastic domain formation on thermal conductivity in Li_2TiGeO_5 ceramics, *J. Therm. Anal. Calorim.*, 2014, **115**, 467–470.

51 E. Corradi, S. V. Meille, M. T. Messina, P. Metrangolo and G. Resnati, Halogen bonding versus hydrogen bonding in driving self-assembly processes, *Angew. Chem., Int. Ed.*, 2000, **39**, 1782–1786.

52 G. Kaur, P. Panini, D. Chopra and A. Roy Choudhury, Structural investigation of weak intermolecular interactions in fluorine substituted isomeric N-benzylideneanilines, *Cryst. Growth Des.*, 2012, **12**, 5096–5110.

53 P. Cardillo, E. Corradi, A. Lunghi, S. V. Meille, M. T. Messina, P. Metrangolo and G. Resnati, The N··· I intermolecular interaction as a general protocol for the formation of perfluorocarbon–hydrocarbon supramolecular architectures, *Tetrahedron*, 2000, **56**, 5535–5550.

54 J. Lombard, T. le Roex and D. A. Haynes, Competition between Hydrogen and Halogen Bonds: The Effect of Solvent Volume, *Cryst. Growth Des.*, 2020, **20**, 7384–7391.

55 Q. J. Shen, H. Q. Wei, W. S. Zou, H. L. Sun and W. J. Jin, Cocrystals assembled by pyrene and 1, 2-or 1,4-diiodotetrafluorobenzenes and their phosphorescent behaviors modulated by local molecular environment, *CrystEngComm*, 2012, **14**, 1010–1015.